

AD\_\_\_\_\_

Award Number: W81XWH-09-1-0053

TITLE: Assessments of Tumor Extracellular pH with PARACEST MRI

PRINCIPAL INVESTIGATOR: VIPUL RAVINDRA SHETH, B.S.E

CONTRACTING ORGANIZATION: Case Western Reserve University  
Cleveland, OH 44106

REPORT DATE: January 2012

TYPE OF REPORT: Annual Summary

PREPARED FOR: U.S. Army Medical Research and Materiel Command  
Fort Detrick, Maryland 21702-5012

DISTRIBUTION STATEMENT: Approved for Public Release;  
Distribution Unlimited

The views, opinions and/or findings contained in this report are those of the author(s) and should not be construed as an official Department of the Army position, policy or decision unless so designated by other documentation.

REPORT DOCUMENTATION PAGE				Form Approved OMB No. 0704-0188	
Public reporting burden for this collection of information is estimated to average 1 hour per response, including the time for reviewing instructions, searching existing data sources, gathering and maintaining the data needed, and completing and reviewing this collection of information. Send comments regarding this burden estimate or any other aspect of this collection of information, including suggestions for reducing this burden to Department of Defense, Washington Headquarters Services, Directorate for Information Operations and Reports (0704-0188), 1215 Jefferson Davis Highway, Suite 1204, Arlington, VA 22202-4302. Respondents should be aware that notwithstanding any other provision of law, no person shall be subject to any penalty for failing to comply with a collection of information if it does not display a currently valid OMB control number. <b>PLEASE DO NOT RETURN YOUR FORM TO THE ABOVE ADDRESS.</b>					
1. REPORT DATE January 2012		2. REPORT TYPE Annual Summary		3. DATES COVERED 1 January 2009 – 31 December 2011	
4. TITLE AND SUBTITLE  Assessments of Tumor Extracellular pH with PARACEST MRI				5a. CONTRACT NUMBER	
				5b. GRANT NUMBER W81XWH-09-1-0053	
				5c. PROGRAM ELEMENT NUMBER	
6. AUTHOR(S)  VIPUL RAVINDRA SHETH  E-Mail: vipul.sheth@case.edu				5d. PROJECT NUMBER	
				5e. TASK NUMBER	
				5f. WORK UNIT NUMBER	
7. PERFORMING ORGANIZATION NAME(S) AND ADDRESS(ES)  Case Western Reserve University Cleveland, OH 44106				8. PERFORMING ORGANIZATION REPORT NUMBER	
9. SPONSORING / MONITORING AGENCY NAME(S) AND ADDRESS(ES) U.S. Army Medical Research and Materiel Command Fort Detrick, Maryland 21702-5012				10. SPONSOR/MONITOR'S ACRONYM(S)	
				11. SPONSOR/MONITOR'S REPORT NUMBER(S)	
12. DISTRIBUTION / AVAILABILITY STATEMENT Approved for Public Release; Distribution Unlimited					
13. SUPPLEMENTARY NOTES					
14. ABSTRACT  In this research project an approach to measure pH by Chemical Exchange Saturation Transfer (CEST) MRI is developed. We describe the characterization of a PARACEST MRI contrast agent, Yb-DO3A-oAA, for pH measurement. The pH measurement is independent of concentration and T1sat relaxation times, and covers a wider pH measurement range than alternative methods. We also developed a new method for fitting PARACEST. To simplify MRI acquisition of CEST spectra a new MRI method was developed, arrayed CEST-FISP. The parameters of this method were optimized for use with PARACEST agents. With this techniques established we translated Yb-DO3A-oAA from in vitro to in vivo use to measure pH in a MDA-MB-231 tumor model and mouse muscle. The pharmacodynamics of Yb-DO3A-oAA were investigated and the fitting algorithm was extended to in vivo tissues.					
15. SUBJECT TERMS Breast Cancer, pH, MRI, PARACEST					
16. SECURITY CLASSIFICATION OF:			17. LIMITATION OF ABSTRACT	18. NUMBER OF PAGES	19a. NAME OF RESPONSIBLE PERSON
a. REPORT	b. ABSTRACT	c. THIS PAGE			USAMRMC
U	U	U	UU	Ā ĩ	19b. TELEPHONE NUMBER (include area code)

**TABLE OF CONTENTS:**

Introduction.....	2
Body.....	2
Key Research Accomplishments.....	8
Reportable Outcomes.....	8
Conclusion.....	9
Future Directions.....	10
References.....	11
Appendix I .....	12
Appendix II.....	46

## INTRODUCTION:

Tumor pH is an important biomarker in cancer. In this research project an approach to measure pH by Chemical Exchange Saturation Transfer (CEST) MRI is developed. We describe the characterization of a PARACEST MRI contrast agent, Yb-DO3A-oAA, for pH measurement. The pH measurement is independent of concentration and T1sat relaxation times, and covers a wider pH measurement range than alternative methods. We also developed a new method for fitting PARACEST spectra. To simplify MRI acquisition of CEST spectra a new MRI method was developed, arrayed CEST-FISP. The parameters of this method were optimized for use with PARACEST agents. With these techniques established we translated Yb-DO3A-oAA from *in vitro* to *in vivo* use to measure pH in a MDA-MB-231 tumor model and mouse muscle. The pharmacodynamics of Yb-DO3A-oAA were investigated and the fitting algorithm was extended to *in vivo* tissues.

## BODY:

*Task 1. To refine our in vivo pH measurements with PARACEST MRI.*

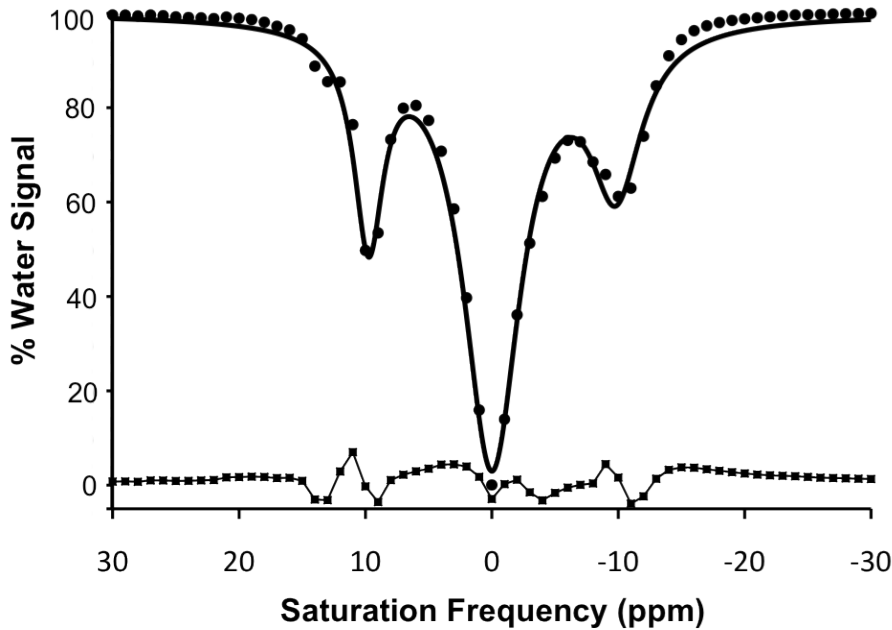


Figure 1 CEST Spectrum of Yb-DO3AoAA

To first characterize our agent, we measured a CEST spectrum, Figure 1, by measuring the water signal after selective saturation at a range of frequencies. Details are provided in Appendix 1 in a manuscript accepted for publication[1]. The CEST spectrum (circles) was fitted with a single function that consisted of a sum of three Lorentzian lines (thick line). The difference between the experimental data and the fitted function (squares connected by a thin line) shows the residual errors of the line fitting process. The CEST spectrum demonstrates two unique exchange groups at -10 and 9 ppm. Details of the fitting process are in appendix 1. We then

used a method of varying the saturation times to calculate the exchange rates of each exchanging group.

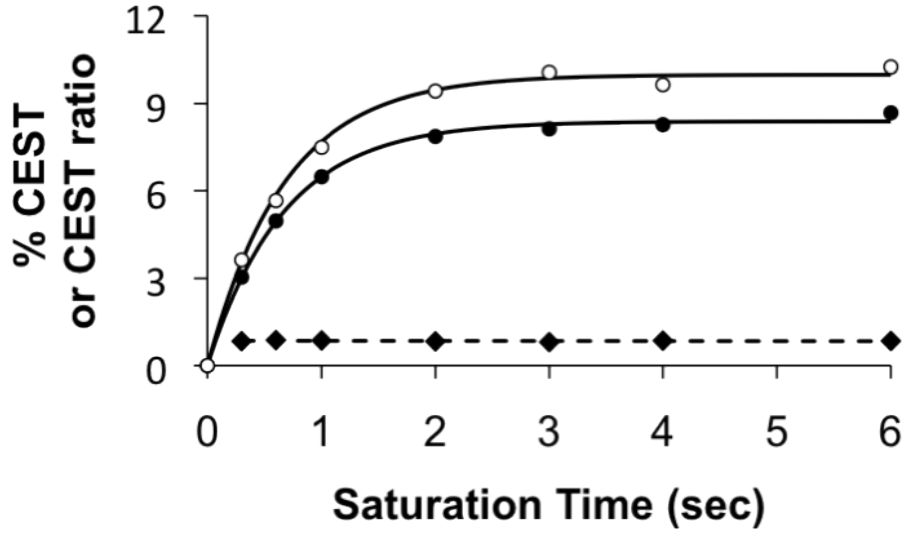


Figure 2 QUEST Method shows % CEST vs Saturation Time (s)

Figure 2 shows the % CEST effects of the amide (filled circles) and amine (unfilled circles) of 30 mM of Yb---DO3A---oAA were measured at pH 6.32 and 38.3 °C using 10  $\mu$ T saturation power. The QUEST equation was fitted to each CEST effect (solid lines) (25). The amide/amine ratio of the CEST effects (diamonds) showed no dependence on the saturation time (the dotted line represents the linear fitting of the ratio of the CEST effects).

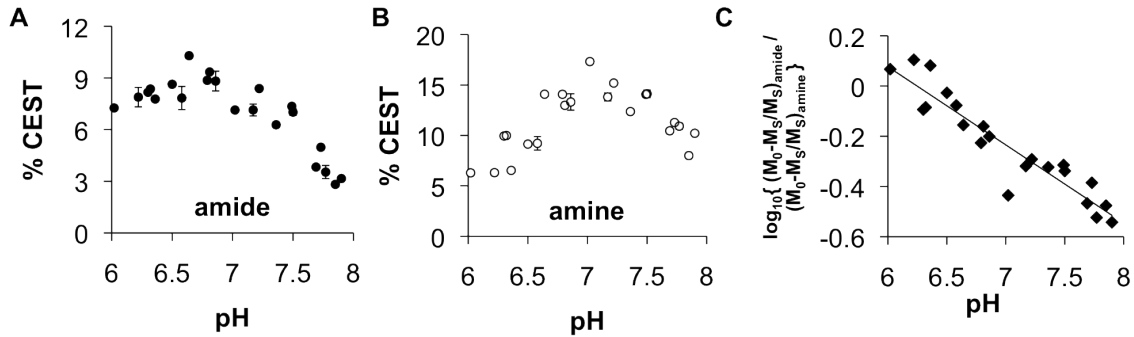
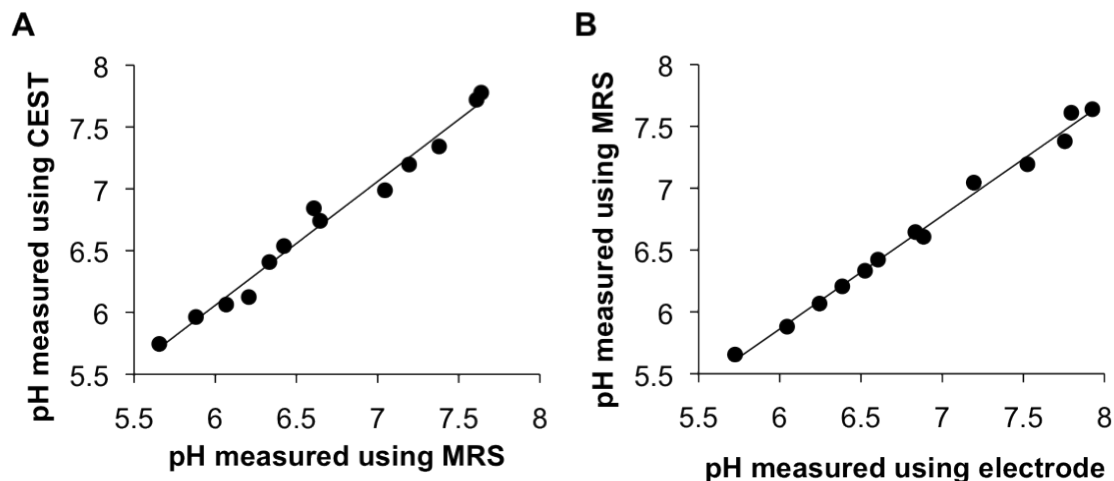


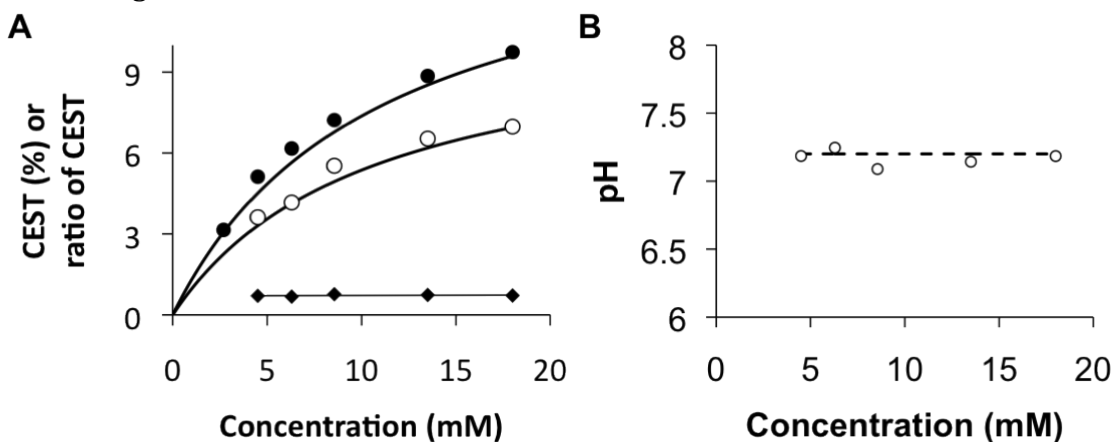
Figure 3 CEST effect versus pH

Figure 3 shows the CEST effect versus pH for each of the exchange groups, amide and amine, of Yb-DO3A-oAA. The % CEST effects of the A) amide and B) amine of Yb-DO3A-oAA were measured at 38.3 °C using 10  $\mu$ T saturation power. Error bars represent the standard deviation of 3 repetitions, and some error bars are smaller than the data symbol. C) The log10 of the ratio of CEST showed an excellent correlation with pH ( $R^2 = 0.88$ ).



**Figure 4 Validation of pH measurements by pH electrode and magnetic resonance spectroscopy**

Figure 4 shows that the pH measured with CEST of Yb-DO3A-oAA had outstanding agreement with the pH measured with MR spectroscopy of IEPA (slope = 1.00,  $R^2 = 0.991$ , standard deviation = 0.089 pH units). B) The pH measured with MR spectroscopy of IEPA had excellent agreement with the pH measured with an electrode (slope = 0.92,  $R^2 = 0.996$ , standard deviation = 0.079 pH units), indicating that the presence of Yb-DO3A-oAA did not affect the chemical shift of IEPA. This allows us to be confident that IEPA measurement of pH is a legitimate control for our CEST agent.



**Figure 5 Dependence of CEST on concentration**

We created Yb-DO3A-oAA with two exchanging groups in order to make our pH measurement concentration independent. Figure 5 shows that our measurement is indeed independent of concentration. The % CEST effects of the amide (filled circles) and amine (unfilled circles) of Yb-DO3A-oAA were measured at pH 7.20 and 37 °C using 10  $\mu$ T saturation power over a range of concentrations. The Hanes---like method was used to fit Eq. 1.1 to the experimental data (curved lines) (26). The ratio of the CEST effects (diamonds) was fit with a linear function to demonstrate

that the ratio is independent of concentration. A similar figure is available in Appendix 1 that demonstrates independence with respect to T1 time of the pH measurement. Further details on all of the above experiments are described in Appendix 1 [1].

This study has shown that pH may be measured using the ratio of two CEST effects from a single PARACEST agent, Yb---DO3A---oAA. The pH can be measured with a precision of 0.206 pH units, and an accuracy of 0.089 pH units. The pH measurement is independent of concentration and T1sat relaxation times, but is dependent on temperature. Yb---DO3A---oAA is an improvement over other ratiometric CEST agents as it's pH range for measurement can full cover the pH range of 6---7.6 that is required to study tumor extracellular pH, provided that the concentration and T1sat relaxation time generate sufficient sensitivity to detect the CEST effects of the agent [1].

**Task 2. To improve diagnoses of tumors and evaluations of anti-tumor chemotherapeutics by measuring tumor pHe with PARACEST MRI:**

An arrayed CEST-FISP pulse sequence was developed to improve PARACEST MRI acquisition time. Sequence parameters were optimized for Yb-DO3AoAA. Details are provided in Appendix 2 [2].

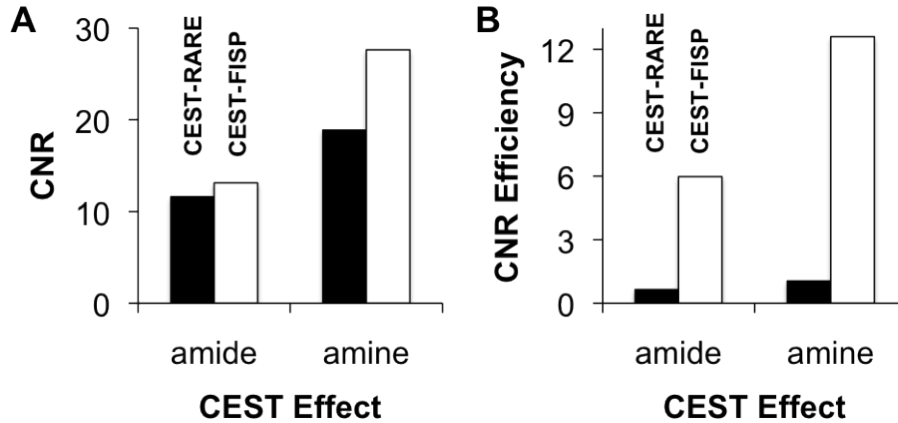


**Figure 6 Comparison of CEST-RARE and CEST-FISP**

The CNR and CNR Efficiency was measured for 22 mM Yb- DO3A-oAA at 37 °C and pH 7.1, using 20  $\mu$ T saturation power for 4.81 seconds with a 300 Hz bandwidth and a 1 msec interpulse delay, and applying a spoiling gradient along the Z axis with 10% gradient power after the saturation period. Figure 6 shows that CEST-FISP detected a greater CNR than CEST-RARE for CEST effects of the amide and amine, and due to the fast acquisition speed of FISP relative to RARE, CEST-FISP had a much greater CNR efficiency than CEST-RARE.

The arrayed CEST-FISP pulse program simplifies acquisition setup and subsequent analysis, and has strong potential to increase CEST experimental throughput that will facilitate future discoveries, further details are available in Appendix 2.

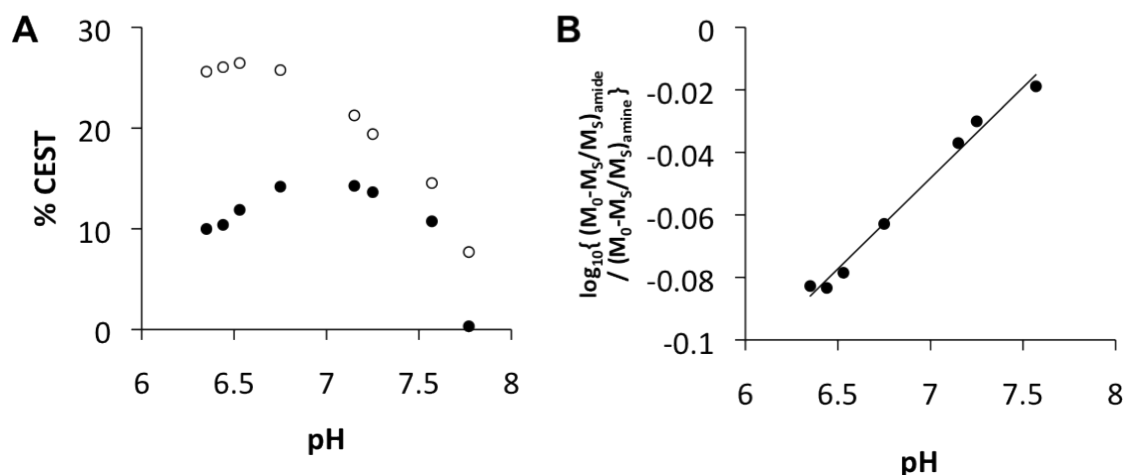


**Figure 7 CEST and pH at 300 MHz**

The next step in acquiring in vivo CEST pH images was to recreate the pH calibration work done in Task 1 at the field strength of the small animal imaging MRI. Figure 7 shows the relationship between CEST effects and pH at 300 MHz for Yb-DO3A-oAA. The % CEST effects of the amide (filled circles) and amine (unfilled circles) of 100 mM Yb-DO3A-oAA were measured at 37 °C using 20  $\mu$ T saturation power. B) The log<sub>10</sub> of the ratio of CEST showed an excellent correlation with pH ( $R^2 = 0.94$ ). The calibration spanned pH 6.35-7.57.



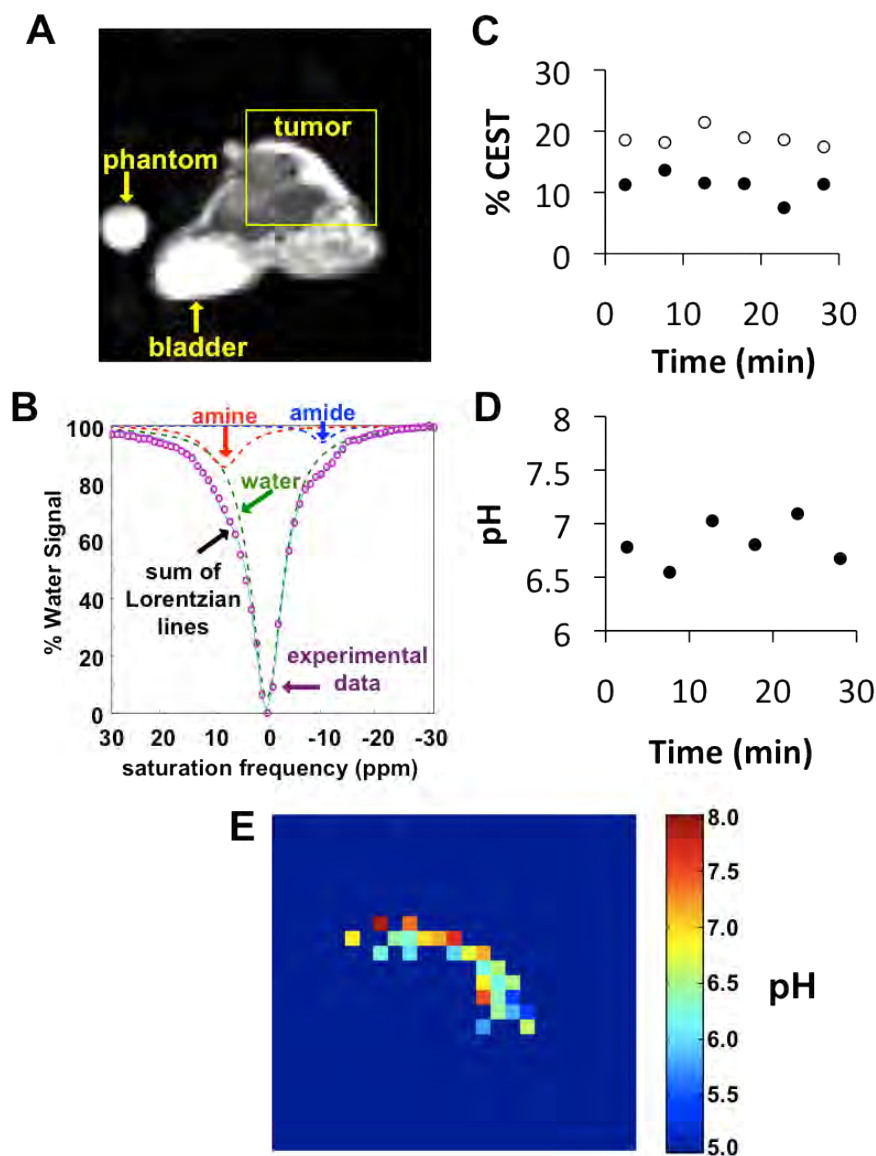


**Figure 8 Measurement of in vivo tumor pH**

Figure 8 demonstrates the successful measurement of tumor pH. A 50  $\mu$ L volume of 100 mM Yb-DO3A-oAA was directly injected into the subcutaneous tumor of a model of MDA-MB-231 mammary carcinoma. A) A CEST---FISP MR image with selective saturation at 30 ppm (i.e., with no saturation of the contrast agent) at 23.0 minutes after injection shows the location of the tumor (yellow box), bladder, and reference phantom. B) The CEST spectrum of the tumor ROI at 23.0 minutes after injection shows CEST effects from the amine and amide. C) The CEST effects of the amide (filled circles) and amine (unfilled circles) showed that the contrast agent remained in the tumor for at least 28.0 minutes. D) The average pH of the tumor was determined from the CEST effects and the CEST-pH calibration (Figure 7). The average of these six measurements was pH 6.82 with a standard deviation of 0.21

pH units. E) The pixel---wise pH map of the tumor ROI at 23.0 minutes shows an average pH of 6.8 and a standard deviation of 0.4. Further details are found in Appendix 2 [2].

### **KEY RESEARCH ACCOMPLISHMENTS:**

- Characterized a PARACEST MRI contrast agent, Yb-DO3A-oAA for pH measurement.
- The pH measurement is independent of concentration and T1sat relaxation times, and covers a wider pH measurement range than alternative methods.
- Developed a new method for fitting PARACEST spectra, that has potential to shorten acquisition times.
- Developed a new MRI method, arrayed CEST-FISP which also shortens acquisition time.
- CEST-FIST parameters were optimized for use with PARACEST agents.
- Translated Yb-DO3A-oAA from *in vitro* to *in vivo* use to measure pH in a MDA-MB-231 tumor model.

### **REPORTABLE OUTCOMES:** Reportable Outcomes for 2011

#### Publications Accepted:

- **Sheth VR**, Liu G, Li Y, Pagel MD. Improved pH measurements with a single PARACEST MRI contrast agent. Contrast Media Mol Imaging. In press.
- **Sheth VR**, Li Y, Chen LQ, Howison CM, Flask CA, Pagel MD. Measuring *in vivo* tumor pHe with CEST-FISP MRI. Magnetic Resonance in Medicine. 2011. epub.

#### Presentation & Abstracts

- **Sheth VR**, Li Y, Chen LQ, Howison CA, Pagel MD. Measuring *in vivo* tumor pHe with a PARACEST MRI contrast agent. Poster Presentation at the Era of Hope, Orlando, FL, USA, Aug 5-8, 2011.
- **Sheth VR**, Li Y, Chen LQ, Howison CA, Pagel MD. Measuring *in vivo* tumor pHe with a PARACEST MRI contrast agent. Poster Presentation at the ISMRM, Montreal, Canada, May 10, 2011.
- Li Y, **Sheth VR**, Liu G, Pagel MD. A self-calibrating PARACEST MRI contrast agent that detects esterase enzyme activity. Poster Presentation at the ISMRM, Montreal, Canada, May 10, 2011.
- Chen LQ, **Sheth VR**, Howison CA, Kuo PH, Pagel MD. Measuring *in vivo* tumor pHe with a DIACEST MRI contrast agent. Poster Presentation at the ISMRM, Montreal, Canada, May 10, 2011.

Funding Applied for Based on Work Supported by This Award:

1R01CA167183-01 (Pagel)

1/1/12-12/31/17

Measuring extracellular pH in pre-clinical tumor models with CEST MRI

This proposal will develop CEST agents and improve CEST MRI methods that detect enzyme activities in pre-clinical cancer models. This proposal received a score in the 5th percentile at the Scientific Review in October 2011, and was approved at the Council Review in January 2012. Final approval and transfer of funds will occur by April 1, 2012.

Degrees Obtained

- MD & PhD degrees from Case Western Reserve University, May 2012

## **CONCLUSION:**

This study has shown that pH may be measured using the ratio of two CEST effects from a single PARACEST agent, Yb-DO3A-oAA. The pH measurement is independent of concentration and T1sat relaxation times. Yb-DO3A-oAA is an improvement over other ratiometric CEST agents as its pH range for measurement can fully encompass the pH range of 6-7.4 that is required to study tumor extracellular pH, provided that the concentration and T1sat relaxation time generate sufficient sensitivity to detect the CEST effects of the agent. The CEST---FISP acquisition protocol dramatically shortens acquisition times and maintains CEST contrast relative to CEST---RARE. The arrayed CEST---FISP pulse program simplifies acquisition setup and subsequent analysis, and has strong potential to increase CEST experimental throughput that will facilitate future discoveries.

In spite of the lower magnetic field strength for MRI studies relative to initial NMR spectroscopy studies, Yb-DO3A-oAA can measure pH throughout the physiological pH range of 6.35---7.57, which is an improvement relative to previously reported methods of PARACEST MRI pH measurement. The *in vivo* pH was measured in tumor and muscle tissues of a MDA-MB-231 tumor model of breast cancer by directly injecting Yb-DO3A-oAA into each tissue.

## **FUTURE DIRECTIONS:**

The primary limitation for Yb---DO3A---oAA and CEST and PARACEST agents in general is limited sensitivity. Changing the chelated lanthanide to Tm or Dy could improve this primarily by increasing the chemical shift of pH dependent exchanging groups. An increased chemical shift would reduce the effects from magnetization transfer interference, B0 and B1 inhomogeneities, and should increase the contrast to noise ratio of the measured CEST effect.

Alternatively, the structure of the chelating compound could be changed to move the amide and amine protons to a position that experiences a higher magnetic susceptibility from the lanthanide, such as the location of the bound water molecule when it is chelated in a basket-like DOTA chelator. Another method to improve sensitivity would be to conjugate multiple (PARA)CEST contrast agents to a macromolecular carrier. Assuming that the CEST effect increases linearly with the number of agents per macromolecule, this method is primarily a way to increase the potential total amount of chelated agents that can be injected at one time.

There are several target applications for using Yb---DO3A---oAA to measure tumor pH. These include measuring tumor pH over time, as a decrease in average tumor pH may signal a transition to more metastatic disease. Acidosis may contribute to the breakdown of the basement membrane and, in metastatic colonization, acidosis is associated with invasion of the colony into the host parenchyma. Tumor cell invasion can be stimulated by acidic conditions *in vitro* and pre---treatment of tumor cells with acid prior to injection leads to increased experimental metastases *in vivo*.

Several pH altering therapies have also been proposed and these therapies could be monitored with a pH sensitive agent like Yb-DO3A-oAA. Bicarbonate treatment to raise tumor pH has been shown to inhibit metastasis in models of breast cancer. The mice undergoing bicarbonate treatment exhibited increased survival and with lower load of lung metastases with no apparent adverse health effects, which suggests that bicarbonate alkalinized tumors without causing prolonged systemic alkalosis.

A low tumor pHe can also affect chemotherapies. The efficacies of weak acid therapies such as the camptothecin analogue CMMDC (7-chloromethyl-10,11-methylenedioxy-camptothecin) can be enhanced by acidic tumor pHe, while an acidic extracellular tumor environment can provide resistance to chemotherapies that act as weak bases such as doxorubicin. Because metastatic breast cancer cells can over express vacuolar H<sup>+</sup>-ATPase proton pumps, a pH-altering therapy such as the proton pump inhibitor esomeprazole can sensitize tumors to the effects of pH-dependent weak-base therapies. Therefore, the tumor pHe may provide early assessments of pH-altering therapies before metastasis has occurred, for predicting efficacies of pH-dependent chemotherapeutics before the chemotherapy is administered to the patient, and for optimizing combination therapies. The tumor pHe is a “theragnostic biomarker” that may provide diagnoses that tailor therapies for individual breast cancer patients.

## REFERENCES:

1. **Sheth VR**, Liu G, Li Y, Pagel MD. Improved pH measurements with a single PARACEST MRI contrast agent. Contrast Media Mol Imaging. In press.

2. **Sheth VR**, Li Y, Chen LQ, Howison CM, Flask CA, Pagel MD. Measuring in vivo tumor pHe with CEST-FISP MRI. *Magnetic Resonance in Medicine*. 2011. epub.
3. **Sheth VR**, Li Y, Chen LQ, Howison CA, Pagel MD. Measuring in vivo tumor pHe with a PARACEST MRI contrast agent. Poster Presentation at the Era of Hope, Orlando, FL, USA, Aug 5-8, 2011.
4. **Sheth VR**, Li Y, Chen LQ, Howison CA, Pagel MD. Measuring in vivo tumor pHe with a PARACEST MRI contrast agent. Poster Presentation at the ISMRM, Montreal, Canada, May 10, 2011.
5. Li Y, **Sheth VR**, Liu G, Pagel MD. A self-calibrating PARACEST MRI contrast agent that detects esterase enzyme activity. Poster Presentation at the ISMRM, Montreal, Canada, May 10, 2011.
6. Chen LQ, **Sheth VR**, Howison CA, Kuo PH, Pagel MD. Measuring in vivo tumor pHe with a DIACEST MRI contrast agent. Poster Presentation at the ISMRM, Montreal, Canada, May 10, 2011.



# Improved pH measurements with a single PARACEST MRI contrast agent

Journal:	<i>Contrast Media and Molecular Imaging</i>
Manuscript ID:	CMMI-10-0087.R1
Wiley - Manuscript type:	Full Paper
Date Submitted by the Author:	n/a
Complete List of Authors:	Sheth, Vipul; Case Western Reserve University, Department of Biomedical Engineering Liu, Guanshu; Kennedy Krieger Institute, F.M. Kirby Research Center for Functional Brain Imaging; Johns Hopkins University, Department of Radiology Li, Yuguo; Case Western Reserve University, Department of Radiology Pagel, Mark; The University of Arizona, Department of Biomedical Engineering
Keyword:	PARACEST, MRI, contrast agent, pH

Improved pH measurements with a single PARACEST MRI contrast agent

Vipul R. Sheth,<sup>1</sup> Guanshu Liu,<sup>2,3</sup> Yuguo Li,<sup>4</sup> Mark D. Pagel<sup>5,6,7</sup>

- 1. Department of Biomedical Engineering, Case Western Reserve University, Cleveland, OH
- 2. F.M. Kirby Research Center for Functional Brain Imaging, Kennedy Krieger Institute, Baltimore, MD
- 3. Department of Radiology, Johns Hopkins University, Baltimore, MD
- 4. Department of Radiology, Case Western Reserve University, Cleveland, OH
- 5. Department of Biomedical Engineering, University of Arizona, Tucson, AZ
- 6. Department of Chemistry and Biochemistry, University of Arizona, Tucson, AZ
- 7. Arizona Cancer Center, Tucson, AZ

Short title: A PARACEST MRI contrast agent measures pH

Keywords: PARACEST, MRI, contrast agent, pH

Corresponding Author:  
Mark D. Pagel  
Associate Professor of Biomedical Engineering and Chemistry & Biochemistry  
Arizona Cancer Center, room 4949  
University of Arizona  
Tucson, AZ 85724-5024  
Tel: (520)-404-7049  
Fax: (520)-626-0395  
email: mpagel@u.arizona.edu

## **Abstract:**

The measurement of extracellular pH has potential utility for assessing the therapeutic effects of pH-dependent and pH-altering therapies. A PARAMagnetic Chemical Exchange Saturation Transfer (PARACEST) MRI contrast agent, Yb-DO3A-oAA, has two CEST effects that are dependent on pH. A ratio derived from these CEST effects was linearly correlated with pH throughout the physiological pH range. The pH can be measured with a precision of 0.21 pH R2.1 units and an accuracy of 0.09 pH units. The pH measurement is independent of concentration and  $T_1$  relaxation times, but is dependent on temperature. Although MR coalescence affects the CEST measurements especially at high pH, the ratiometric analysis of the CEST effects can account for incomplete saturation of the agent's amide and amine that results from MR coalescence. Provided that an empirical calibration is determined with saturation conditions, magnetic field strength, and temperature that will be used for subsequent studies, these results demonstrate that this single PARACEST MRI contrast agent can accurately measure pH.

## **1. Introduction**

Substantial evidence indicates that some tumor microenvironments become hypoxic, which leads to acidic extracellular pH (pHe), which then changes extrinsic cellular interactions that lead to tumor malignancy (1,2). However, the timing of changes in tumor pHe with respect to tumor progression and metastatic potential is largely unknown. Therapies that alkalinize tumor pHe have been suggested to reduce malignancy (3-5). Yet the effects of pH-modulating therapies on pHe in tumors and normal tissues must be longitudinally evaluated when this class of anti-cancer therapies is investigated. Therefore, there is an imperative need for a clinically relevant, high resolution, noninvasive imaging methodology for measuring tumor pHe.

Microelectrodes, optical imaging, electron paramagnetic resonance imaging, PET imaging and magnetic resonance spectroscopy have been used to measure tumor pHe, but these methods suffer from coarse spatial resolution that cannot evaluate tumor microenvironments (6-11). Hyperpolarized  $^{13}\text{C}$  MRS for measuring tumor pHe has recently attracted interest, but this technique requires a hyperpolarization system and a  $^{13}\text{C}$  transceiver coil that are unavailable in R4.5 most radiology clinics, measures a weighted average of intracellular and extracellular pH, and



also suffers from coarse spatial resolution (12). Magnetic Resonance Imaging (MRI) can evaluate the entire tumor volume with fine spatial resolution, and therefore is an improvement relative to these other methods. Some MRI contrast agents can change their  $T_1$  relaxivities in a pH-dependent manner, but the change in  $T_1$  relaxation time caused by a pH-responsive MRI contrast agent is also dependent on the concentration of the agent (11, 13-16). Serial injections of multiple contrast agents, and/or including a  $T_2$ - or  $T_2^*$ -relaxation MRI measurement to account for agent concentration may be complicated (17,18). More recently, a pH-dependent  $T_1$ -relaxation MRI contrast agent has been modified to carry  $^{18}\text{F}$  for PET imaging to quantify agent concentration (19). Yet using two imaging modalities may be problematic, and the ~1 mm spatial resolution of PET imaging is relatively coarse. Therefore, methods that measure tumor pHe a relaxation-based MRI contrast agent are challenging.

MRI contrast agents that are detected via Chemical Exchange Saturation Transfer (CEST) have also been employed to measure pH. One of the first CEST agents to be characterized, 5,6-dihydrouracil, has two amides that produce two CEST effects (Figure 1A) (20). A ratiometric comparison of the two CEST effects was shown to be correlated with pH between 6.2-7.0 at 300 MHz magnetic field strength. Another CEST agent, N,N'-bis(2,3-dihydroxypropyl)-2,4,6-triiodo-5[(methoxyacetyl)amide]-1[N-methyl]-1,3-benzenedicarboxamide (Iopamidol), also has two amides that produce two CEST effects, which can be used to measure pH over a similar range of 6.0-7.0 at 300 MHz (Figure 1B) (21). For each of these CEST agents, the chemical shifts of the amides are similar and near the chemical shift of water, so that selective detection and quantification of each CEST effect can be technically difficult.

Paramagnetic CEST (PARACEST) contrast agents contain a lanthanide ion that greatly shifts the MR frequency of the exchangeable protons from the MR frequency of water, which expands the range of MR frequencies that can generate a CEST effect (22). This expanded frequency range facilitates the selective detection of two CEST effects from the same contrast agent. A series of PARACEST agents that use 1,4,7,10-tetraazacyclododecane,N,N',N'',N'''-tetraacetic acid (DOTA-Gly<sub>4</sub>) to chelate Pr(III), Eu(III) or Nd(III) possess pH-responsive and pH-unresponsive CEST effects from an amide and metal-bound water, respectively (Figure 1C) (23,24). A ratio of the two CEST effects can then be used to measure pH over a range of 6.5-7.5 at 300 MHz.

However, very high saturation powers are required to detect the PARACEST effect from the metal-bound water due to fast exchange rates at physiological temperature, so that these agents cannot be safely applied to measure in vivo tumor pH. More recently, the ratio of two CEST effects of a PARACEST agent with a different ligand coordination cage, Yb(III) chelate of 10-(2-hydroxypropyl)-1,4,7,10-tetraazacyclododecane-1,4,7-triacetic acid (Yb-HPDO3A), has been shown to measure pH at moderate saturation powers. This indicates that a single PARACEST agent for eventual in vivo studies of tissue pH may be feasible (25). Another PARACEST agent with a single CEST effect has been shown to have a pH-dependent chemical shift, which can be used to measure pH without requiring a measurement of the agent's concentration, further expanding the functionality of PARACEST agents for pH measurements (26).

We have previously reported a PARACEST MRI contrast agent, Yb<sup>3+</sup>-1,4,7,10-tetraazacyclododecane-1,4,7-triacetic acid, 10-o-aminoanilide (Yb-DO3A-oAA), that has two CEST effects at chemical shifts that are selectively detectable at reasonable saturation powers for pre-clinical studies (Figure 1D) (27,28). These previous studies indicated that the amide and amine of this agent produce CEST effects with different magnitudes at different pH. Therefore, we hypothesized that the ratiometric comparison of these two CEST effects may also be correlated with pH. Furthermore, our previous studies of Yb-DO3A-oAA showed that the ratio of the two CEST effects was independent of concentration and T<sub>1</sub> relaxation time, but was dependent on temperature. For comparison, the previous studies of 5,6-dihydrouracil, Iopamidol, and lanthanide chelates of DOTA-Gly<sub>4</sub> did not investigate the dependence of the pH measurements on these other conditions, so that the accuracy of these methods during practical applications is unknown. Therefore, we investigated the influence of these other conditions to evaluate if the single PARACEST MRI contrast agent, Yb-DO3A-oAA, can accurately measure pH.

## **2. Theory**

### **2.1. CEST and pH**

CEST is typically reported as the decrease in water signal during selective saturation of the contrast agent, relative to the water signal without selective saturation of the agent while accounting for direct saturation of water (Eq. [1]). To describe chemical exchange phenomena,

the Bloch equations can be modified to account for chemical exchange within a two pool model (29). These equations can be simplified by assuming that complete saturation of the contrast agent is achieved, saturation is achieved instantaneously, and that direct saturation of water protons is negligible (Eq. [2]). The ratio of two CEST effects from the same agent are a function of only the number of exchangeable protons and the chemical exchange rates, assuming that the  $T_{1sat}$  relaxation time and concentration of water involved in chemical exchange is the same for each exchangeable proton (Eq. [3]). The chemical exchange behavior of amides and amines are known to be base-catalyzed (Eq. [4]) (30). Therefore, the ratio of the CEST effects can be related to pH (Eq. [5]) (31).

$$\% \text{ CEST} = 1 - \frac{M_s}{M_0} \tag{1}$$

where

$M_s$ : water magnetization with selective saturation of the agent, and potentially with partial direct saturation of bulk water

$M_0$ : water magnetization without selective saturation of the agent, but potentially with partial direct saturation of bulk water

$$\frac{M_s}{M_0} = \frac{1}{1 + T_{1sat} k_{CA} \left( \frac{n_{CA} [CA]}{n_{H_2O} [H_2O]} \right)} \tag{2}$$

where

$k_{CA}$ : chemical exchange rate of a proton from the agent to water

$T_{1sat}$ :  $T_1$  relaxation time in the presence of selective saturation

$n_{CA}, n_{H_2O}$ : number of magnetically equivalent exchangeable protons on the contrast agent and water molecule, respectively

$[CA], [H_2O]$ : concentration of the contrast agent and water, respectively

Assuming that  $[CA]$ ,  $[H_2O]$ , and  $T_{1sat}$  are equal for the two CEST effects,

$$\frac{\left[ (M_0 - M_s) / M_s \right]_{CA1}}{\left[ (M_0 - M_s) / M_s \right]_{CA2}} = \frac{n_{CA1} k_{CA1}}{n_{CA2} k_{CA2}} \quad [3]$$

$$k_{CA} = k_0 + k_a 10^{-pH} + k_b 10^{-(pK_w - pH)} \quad [4A]$$

where

$k_0$ : spontaneous chemical exchange rate

$k_a$ : acid-catalyzed chemical exchange rate

$k_b$ : base-catalyzed chemical exchange rate

$pK_w$ : ionization constant of water,  $K_w$ .  $pK_w = 15.4$  at  $37.0^\circ\text{C}$  (32)

For base-catalyzed chemical exchange,  $k_a$  is negligible and Eq. [2.8A] can be simplified:

$$k_{CA} = k_0 + k_b 10^{-(pK_w - pH)} \quad [4B]$$

$$\frac{\left[ (M_0 - M_s) / M_s \right]_{CA1}}{\left[ (M_0 - M_s) / M_s \right]_{CA2}} = \frac{n_{CA1} \left( k_0 + k_b 10^{-(pK_w - pH)} \right)}{n_{CA2} \left( k_0 + k_b 10^{-(pK_w - pH)} \right)} \quad [5]$$

## 2.2. The line shapes of a CEST spectrum

An alternative modification of the Bloch equations to account for chemical exchange within a two pool model can relate the CEST effect to the MR chemical shift of the selective saturation (Eq. [6]). As with Eq. [2], this modification assumes complete and instantaneous saturation of the contrast agent, and that direct saturation of water protons is negligible. Combining Eqs. [1] and [6] shows that the CEST spectrum has a Lorentzian line shape in aqueous solutions (Eqs. [7A-7G]) (33).

$$\frac{M_s}{M_0} = \frac{1 + \left[ (sf - \omega_0) T_{2sat} \right]^2}{1 + \left[ (sf - \omega_0) T_{2sat} \right]^2 + \omega_{1sat}^2 T_{1sat} T_{2sat}} \quad [6]$$

$$1 - \frac{M_s}{M_0} = 1 - \frac{1 + \left[ (sf - \omega_0) T_{2sat} \right]^2}{1 + \left[ (sf - \omega_0) T_{2sat} \right]^2 + \omega_{1sat}^2 T_{1sat} T_{2sat}} \quad [7A]$$

$$1 - \frac{M_s}{M_0} = 1 - \frac{\frac{\omega_{1sat}^2 T_{1sat}}{T_{2sat}}}{(sf - \omega_0)^2 + \left[ \frac{1}{T_{2sat}^2} + \frac{\omega_{1sat}^2 T_{1sat}}{T_{2sat}} \right]} \quad [7B]$$

where

sf: the MR chemical shift of the selective saturation

$\omega_0$ : the MR chemical shift of the exchangeable proton of the CEST agent

$\omega_{1sat}$ : saturation power (in units of Hz)

$T_{1sat}, T_{2sat}$ :  $T_1$  and  $T_2$  relaxation times of water in the presence of saturation

Define:

$$w = \frac{1}{T_{2sat}^2} + \frac{\omega_{1sat}^2 T_{1sat}}{T_{2sat}} \quad [7C]$$

$$A = \frac{\omega_{1sat}^2 T_{1sat} T_{2sat}}{1 + \omega_{1sat}^2 T_{1sat} T_{2sat}} \quad [7D]$$

Substituting Eqs. [7C] and [7D] into Eq. [7B], and expanding Eq. [7B] to account for two CEST effects of Yb-DO3A-oAA and the direct saturation of water, results in a sum of three Lorentzian line shapes:

$$1 - \frac{M_s}{M_0} = \frac{A_1 w_1^2}{(sf - \omega_1)^2 + w_1^2} + \frac{A_2 w_2^2}{(sf - \omega_2)^2 + w_2^2} + \frac{A_3 w_3^2}{(sf - \omega_3)^2 + w_3^2} \quad [7E]$$

where

$A_{1,2,3}$ : the area of the Lorentzian line

$w_{1,2,3}$ : the line width at half height of the Lorentzian line

$\omega_{1,2,3}$ : the maximum of the Lorentzian line

### 3. Results and Discussion

#### 3.1. The CEST Effects of Yb-DO3A-oAA

A 30 mM sample of Yb-DO3A-oAA at pH 7.3 and 38.3 °C showed a 33.8% CEST effect at -9.80 ppm and a 44.3% CEST effect at +9.75 ppm (Figure 2). This CEST effect at -9.80 ppm was assigned to the amide based on CEST studies of similar Yb(III) chelates with amides at the same

structural position (34). The other CEST effect was assigned to the amine based on evidence from previous reports (27,28). NMR spectra in 10% D<sub>2</sub>O and ~100% D<sub>2</sub>O revealed that the exchangeable protons had chemical shifts of +9.60 and -8.95 ppm, which were close to the MR frequencies used to detect the CEST effects (Figure S1).

Each CEST spectrum was fit with a function that consisted of a sum of three Lorentzian lines (Eq. [7G]). The residuals of the fitting routine showed non-negligible errors at the saturation frequencies of the CEST effects for the amide and amine (Figure 2). Yet the Lorentzian lines that represented the CEST effects of the amide and amine had ranges of 19.7 ppm and 12.3 ppm, respectively (the range of each CEST effect was defined as the width of the "base" of the Lorentzian line which lies at the signal amplitude that is equal to the standard deviation of the residual errors of the Lorentzian line fitting). These ranges indicated that the fitting of each CEST effect depended on more experimental data points than just the experimental data point at -10 and 10 ppm, suggesting that the Lorentzian line fitting may generate more accurate measurements than relying on single experimental data point for each CEST effect.

The time to reach steady state saturation depends on the chemical exchange rate and the T<sub>1</sub> relaxation rates of the agent and water (35). The time to reach steady state saturation for each CEST effect was measured by varying the saturation time while also adjusting the delay time between acquisitions to maintain constant relaxation effects (Figure 3). These results demonstrate that a saturation time of 2.5 seconds was sufficient to reach steady state. A saturation time greater than 2.5 seconds was used for all subsequent experiments. In addition, the ratio of the CEST effects was invariant with respect to saturation time.

### 3.2. The measurement of pH with Yb-DO3A-oAA

The CEST effect from the amide group increased slightly from pH 6 to pH 6.6 before decreasing at higher pH values (Figure 4A). The CEST effect from the amine group increased from pH 6 to pH 7.2, and then decreased at higher pH values (Figure 4B). As suggested by Eq. [5], the log<sub>10</sub> of the ratio of the CEST effects was found to be linearly dependent on pH (Figure 4C). The pH of subsequent studies was determined from this correlation,  $\text{pH} = 6.34 - 2.82 [\log_{10}\{((M_0 - M_S)/M_0)_{\text{amide}} / ((M_0 - M_S)/M_0)_{\text{amine}}\}]$ . Although the magnitude of the CEST effect that can be

determined with good probability is dependent on the noise level of the MR results, a 5% CEST effect is generally accepted as a minimum threshold for most MRI applications (27,36). The CEST effects are greater than 5% through a pH range of 6.0-7.6 under the experimental conditions of this study.

To assess the precision of the pH measurements from the CEST effects of Yb-DO3A-oAA, the standard deviation of the experimental pH measurements relative to the linear regression was determined to be 0.21 pH units. This level of precision is an upper limit of uncertainty, because the "gold standard" pH electrode has an accuracy of approximately 0.05 pH units. No statistically significant difference was observed for the accuracy of measuring low pH vs. high pH values.

To assess the accuracy of this CEST method, the pH of each sample was also measured using MR spectroscopy of IEPA (Figure S2) (37). The comparison of pH measurements from both methods showed outstanding agreement throughout the entire pH range, with a slope of 1.00, a  $R^2$  correlation coefficient of 0.99, and a standard deviation of 0.09 pH units (Figure 5A). A paired t-test assuming unequal variances indicated that the pH measurements by IEPA and PARACEST are statistically indistinguishable ( $p=0.29$ ) (38). Although lanthanide ions can act as chemical shift agents, the presence of Yb-DO3A-oAA did not affect the pH measurements with IEPA as compared with a pH electrode (Figure 5B). Although IEPA can act as a pH buffer, this buffering is not expected to influence the CEST measurements of Yb-DO3A-oAA.

**3.3. Conditions that may affect pH measurements with Yb-DO3A-oAA**

The CEST effects of the amine and amide of Yb-DO3A-oAA each increased with increasing concentration (Figure 6A). In theory, the chemical exchange of the amide, amine and water should be modeled as a three-pool system. However, Eq. [2] was fit to the experimental data using a Hanes-like analysis method, which follows a two-pool model in which the two pools are water and one type of exchangeable proton on the agent (Figure 6B; 39). Because this Hanes-like analysis showed a linear fit to the experimental data ( $R^2 = 0.89$  and  $0.94$  for the amine and amide, respectively), both chemical exchange processes can be approximated as a two-pool model. In practice, the amide had negligible effect on the amine-water exchange process, and

the amine had negligible effect on the amide-water exchange process, within the tested concentrations of contrast agent and experimental precision of this analysis. More importantly, the ratio of the CEST effects was not influenced by the concentration of the agent. Thus, the accuracy of the pH measurement was not influenced by concentration (Figure 6C).

Both CEST effects of Yb-DO3A-oAA were dependent on  $T_1$  relaxation time (Figure 7A). However, the ratio of the CEST effects was only marginally dependent on  $T_1$ . Thus, the accuracy of the pH measurement was not influenced by relaxation time (Figure 7B). The  $T_1$  relaxation times of tumor tissues in pre-clinical models at 7 T magnetic field strength is typically 2 seconds, which is longer than the range of this minimum  $T_1$  relaxation times in this study. However, longer relaxation times are not expected to change these results.

The CEST effects of Yb-DO3A-oAA were dependent on temperature (Figure 8A). Unfortunately, the ratio of the CEST effects was also dependent on temperature, so that the measurement of pH using CEST was also dependent on temperature with a dependence of 0.068 pH units per °C (Figure 8B). A similar co-dependence on temperature and pH was recently reported for another PARACEST agent, Yb-HPDO3A (25). Fortunately, physiological temperature can easily be maintained at  $37.0 \pm 0.2$  °C in pre-clinical tumor models during MRI studies that use commercially-available physiological monitoring systems. A  $\pm 0.2$  °C variation in temperature will cause a  $\pm 0.014$  variation in the pH measurement, which is negligible compared to other sources of variation that affect precision. Similar maintenance of stable temperature in patients may be required for clinical translation of pH measurements using CEST MRI.

### 3.4. The relationship between CEST and pH for Yb-DO3A-oAA

To further investigate the relationship between CEST and pH for Yb-DO3A-oAA, the QUantifying Exchange using Saturation Time (QUEST) method was used to measure the chemical exchange rates of the amide and amine throughout the physiological pH range (Figure 9) (35). The chemical exchange rates determined by the QUEST method did not match Eq. [4B], as the exchange rates did not continuously increase with increasing pH. As shown in Figure 2, selective saturation at the chemical shifts of the amide and amine also resulted in direct



saturation of some water. However, this direct saturation of water was approximately the same for all pH values (data not shown), so that direct water saturation does not explain the inconsistent, pH-dependent results of the QUEST study. Instead, only a fraction of the contrast agent concentration appears to be saturated, and this fraction of saturated agent appears to be dependent on pH. The same conclusion was reached during initial studies of the QUEST method (35). R4.15  
R2.4.2,  
R3.3

More specifically, the CEST effect requires that the chemical exchange rate is less than the chemical shift difference between the contrast agent and water ( $k_{CA} < \omega_0$ ). At a low pH of 6.02, the  $k_{CA}$  for the amide and amine (340 and 125 Hz, respectively) are negligible relative to  $\omega_0$  for each group (~3,000 Hz at 300 MHz magnetic field strength, respectively). At high pH,  $k_{CA}$  increases to values greater than 941 and 182 Hz for the amide and amine, respectively, which is still less than  $\omega_0$  but is no longer negligible relative to  $\omega_0$ . A non-negligible  $k_{CA}$  causes MR coalescence of the chemical shifts of the exchangeable protons of the contrast agent and water (40). This MR coalescence at higher pH is supported by the monotonic change in chemical shift and increase in the width of the Lorentzian line for the CEST effect of the amide as pH is increased (Figure 10). A non-negligible  $k_{CA}$  results in a non-negligible amount of protons on the contrast agent that are not saturated under steady state conditions. Because  $k_{CA}$  of the amide becomes non-negligible at lower pH values than the  $k_{CA}$  of the amine, the concentrations of the saturated amide and saturated amine are not equal. Therefore, Eq. [3] must be modified (Eq. [8]).

$$\frac{\left[ (M_0 - M_s) / M_s \right]_{CA1}}{\left[ (M_0 - M_s) / M_s \right]_{CA2}} = \frac{n_{CA1} k_{CA1} [CA]_{1,sat}}{n_{CA2} k_{CA2} [CA]_{2,sat}} \quad [8]$$

Despite the concern that the concentrations of the saturated amide and saturated amine are not equal, Figure 4C shows that the  $\log_{10}$  of the ratio of CEST effects is a linear function of pH. A  $\log_{10}$  representation of Eq. [8] shows that the effects of  $n_{CA}$ ,  $k_{CA}$  and  $[CA]_{sat}$  can each be independently evaluated (Eq. [9]). Because  $n_{CA}$  is independent of pH, the first term of this  $\log_{10}$  equation only contributes to the y-intercept of Figure 5C. Because  $\log_{10}(k_{CA})$  is linearly dependent on pH (Eq. [3B]), the second term contributes to both the y-intercept and slope of

Figure 4C. Similarly, the third term must behave as one of the first two terms to maintain a linear relationship shown in Figure 4C, so that the  $\log_{10}$  ratio of the concentrations of saturated amide and saturated amine is invariant with respect to pH or linearly dependent on pH. A potential pitfall of this analysis method is the use of logarithmic functions that temper the appearance of non-linearity, which reduces the sensitivity of this method to variances in the ratio of concentrations of the saturated amine and amide. Still, this more sophisticated analysis provides qualitative evidence that the concentration of the saturated contrast agent does not affect the pH measurement, so that this single contrast agent can accurately measure pH without concern for pharmacokinetics that change the concentration of the agent within in vivo tissues.

$$\log_{10} \left\{ \frac{\left[ \frac{(M_0 - M_s)}{M_s} \right]_{CA1}}{\left[ \frac{(M_0 - M_s)}{M_s} \right]_{CA2}} \right\} = \log_{10} \left\{ \frac{n_{CA1}}{n_{CA2}} \right\} + \log_{10} \left\{ \frac{k_{CA1}}{k_{CA2}} \right\} + \log_{10} \left\{ \frac{[CA]_{1,sat}}{[CA]_{2,sat}} \right\} \quad [9]$$

Incomplete saturation of the amide and amine may be a potential advantage. As shown in Figure 3, the CEST effects Yb-DO3A-oAA showed that saturation reached a steady-state after 2.5 seconds of saturation time. Yet even shorter experiment times are an important advantage for in vivo studies. The ratiometric,  $\log_{10}$  calibration method for pH measurements in this study offers one such opportunity to shorten saturation time, because the ratio of the two CEST effects was invariant with respect to saturation time (Figure 3), and therefore Eq. [9] can still be used to relate the CEST effects to pH. If shorter saturation times are used, an empirical CEST-pH calibration (Figure 4C) should still be performed with these new conditions to account for differences in incomplete saturation of the amide and amine. The method of fitting a function of Lorentzian lines to the CEST spectra offers another opportunity to shorten saturation time. Unlike other fitting methods that require an understanding of the concentration of saturated contrast agent, the Lorentzian line fitting method does not include a term for concentration (Eq. [7]), so that incomplete saturation does not affect this analysis.

Figures 4A, 4B, and 9 show that MR coalescence becomes increasingly important as pH is increased. Because MR coalescence is dependent on magnetic field strength, a calibration of a CEST agent's dependence on pH must be empirically determined using the magnetic field that will be employed for subsequent pH studies. New contrast agents with exchangeable protons that

have larger chemical shifts than Yb-DO3A-oAA may not require an empirical calibration at each high magnetic field strength if  $k_{CA}$  is negligible relative to  $\omega_0$  throughout the physiological pH range.

Translation of this contrast agent and CEST MRI methodology to in vivo studies of pH will need to consider the effects of  $B_0$  and  $B_1$  inhomogeneities, magnetization transfer effects,  $T_2$  relaxation effects that are related to chemical exchange, and compartmentalization of the PARACEST agent in the vasculature, interstitial space, and intracellular space. This report provides evidence that this PARACEST agent and CEST MRI methodology may address these challenges to provide in vivo measurements of tissue pH. In particular, the pH measurements should be independent of the agent's concentration in each tissue compartment and the tissue's  $T_1$  relaxation time. A Lorentzian line fitting procedure may be used to account for  $B_0$  and  $B_1$  inhomogeneities. The CEST effects at +10 and -10 ppm are symmetric about the water resonance, so that magnetization transfer and  $T_2$  relaxation effects may equally influence both CEST effects so that the CEST ratio is unaffected. Our research program is conducting preliminary studies to investigate in vivo pH measurements with this PARACEST agent and CEST MRI methodology (41).

**4. Conclusions**

This study has shown that pH may be measured using the ratio of two CEST effects from a single PARACEST agent, Yb-DO3A-oAA. The pH can be measured with a precision of 0.21 pH units, and an accuracy of 0.09 pH units. The pH measurement is independent of concentration and  $T_1$  relaxation times, but is dependent on temperature. Although MR coalescence affects the CEST measurements at high pH, the ratiometric analysis of the CEST effects can account for incomplete saturation of the agent's amide and amine that results from MR coalescence. However, the effect of MR coalescence requires an empirical calibration of CEST and pH at each magnetic field strength.

**5. Experimental**

**5.1. Sample Preparation**

DO3A-oAA was synthesized using a previously published procedure (28). Samples used in each study were prepared in approximately 25 mM piperazine-N,N'-bis(2-ethanesulfonic acid) (PIPES buffer) which were titrated to pH values using 1-10  $\mu$ L of 6 N NaOH. These solutions were then used to create samples with final volumes of 600  $\mu$ L and concentrations of 30 mM Yb-DO3A-oAA, 40 mM 2-imidazole-1-yl-3-ethoxycarbonyl propionic acid (IEPA), 10 mM trimethylsilyl propionate (TSP), and 10% D<sub>2</sub>O, unless noted otherwise. IEPA was included to validate pH using MR spectroscopy (37), TSP was included to calibrate the MR chemical shift scale, and D<sub>2</sub>O was included to optimize magnetic field homogeneity and monitor field drift. Concentrations of Yb-DO3A-oAA were corrected to reflect that concentrations of exchangeable protons are functionally reduced due to the presence of D<sub>2</sub>O. To study the effect of T<sub>1</sub> relaxation on pH measurements, microliter amounts of 2 mM Gd-{2-[bis[2-(carboxylatomethyl)-(methylcarbamoylmethyl)amino]ethyl]amino]acetate} (Gadodiamide, Omniscan®) were added to some samples. Inductively coupled plasma mass spectrometry (ICP-MS) confirmed Yb concentrations. The pH of each solution was measured using a calibrated pH electrode and corrected for temperature effects (42).

## **5.2. NMR Methods**

All CEST experiments were performed using a 600 MHz Varian Inova NMR spectrometer with an inverse cryoprobe. Samples were analyzed at 38.3 °C unless otherwise noted. The probe was tuned to each sample, the magnet was automatically shimmed using gradient shimming, and the 90 degree pulse length was measured. A continuous wave presaturation pulse was used to create CEST. To investigate steady-state saturation, a series of saturation times of 0.3, 0.6, 1, 2, 3, 4, and 6 seconds were tested while maintaining a total time for each saturation and acquisition of 7 seconds to maintain consistent relaxation effects. Subsequent CEST studies were performed with a saturation time that was greater than 2.5 seconds. CEST spectra were acquired with a saturation frequency set at 30 ppm to -30 ppm in 1 ppm increments, using a saturation power of 10  $\mu$ T and a saturation bandwidth of 1 ppm (Figure 2). Each scan was averaged 4 times. The temperature of the samples was calibrated by measuring the separation of resonances of neat methanol and ethylene glycol samples between 25 °C and 40 °C (43). T<sub>1</sub> relaxation times were measured with a standard inversion-recovery pulse sequence (44).

NMR spectroscopy of IEPA was performed at 37.0 °C using a Bruker DRX600 NMR spectrometer (Figure S2). A presaturation sequence was used for water suppression. The chemical shifts of the spectra were calibrated by setting the resonance of TSP to 0.0 ppm. The pH was determined from the chemical shift of the H<sub>2</sub> proton as described previously (37,45).

**5.3. Lorentzian Line Fitting**

CEST spectra were fit using a model function of three Lorentzian lines in Matlab R2009B (Eq. [7G]) to measure each CEST effect (Eq. [1]). The value of  $M_0$  for the amine was determined from the value at  $+\omega_0$  (the MR frequency of the amine's maximum CEST effect) for the Lorentzian line that is centered at approximately 0 ppm. A similar procedure was used to determine  $M_0$  for the amide. This method is different from the commonly used method that determines  $M_0$  by measuring the magnitude of the water signal at  $-\omega_0$  (46). This other method assumes that the CEST spectrum is symmetric about the water's chemical shift in the absence of an exchanging chemical group. Other methods have also been described that characterize the CEST effect, but these other methods also rely on the symmetry assumption (47). In the case of Yb-DO3A-oAA, this assumption is not valid because each CEST effect at  $\omega_0$  is close to  $-\omega_0$  for the other CEST effect. Thus a simple comparison would not accurately measure the CEST effect due to the individual exchanging group.

**5.4. Exchange Rate and PARACEST**

Chemical exchange rates were measured for the CEST effects of Yb-DO3A-oAA by using the QUEST method (35). The analytical method derived from the Bloch equations that include chemical exchange was used to analyze the relationship between CEST and saturation time, which was accomplished by using a least squares nonlinear curve fitting routine in Matlab R2009B (Mathworks, Natick, MA).

**Acknowledgements**

This work was supported by the Arizona Cancer Center, the Case Center for Imaging Research and the National Cancer Institute under grants CA110943, CA 023074, CA 017094 and CA133455-01. VRS was supported through the US Army Medical Research and Materiel Command under grant no. W81XWH-09-1-0053 and in part by the CWRU MSTP under NIH

grant no. T32 GM007250. The authors thank Dr. Paloma Ballesteros of the Departamento de Química Orgánica y Biología, Facultad de Ciencias, Universidad Nacional de Educación a Distancia, Madrid, Spain for donating IEPA.

References

1. Warburg O. 1956; On the origin of cancer cells. *Science* 123:309-314.

2. Gillies RJ, Gatenby RA. Hypoxia and adaptive landscapes in the evolution of carcinogenesis. *Cancer Met. Rev.* 2007; 26: 311-317.

3. Raghunand N, He X, van Sluis R, Mahoney B, Baggett B, Taylor CW, Paine-Murrieta G, Roe D, Bhujwala ZM, Gillies RJ. Enhancement of chemotherapy by manipulation of tumor pH. *Br. J. Cancer*, 1999; 80(7): 1005-1011.

4. Mahoney BP, Raghunand N, Baggett B, Gillies RJ. Tumor acidity, ion trapping and chemotherapeutics. I. Acid pH affects the distribution of chemotherapeutic agents in vitro. *Biochem. Pharmacol.* 2003; 66(7): 1207-1218.

5. Raghunand N, Mahoney BP, Gillies RJ. Tumor acidity, ion trapping and chemotherapeutics. II. pH-dependent partition coefficients predict importance of ion trapping on pharmacokinetics of weakly basic chemotherapeutic agents. *Biochem. Pharmacol.* 2003; 66(7): 1219-1229.

6. Thistlethwaite AJ, Leeper DB, Moylan DJ, Nerlinger RE. pH distribution in human tumors. *Int J. Radiation Oncol. Biol. Phys.* 1985; 11(9): 1647-1652.

7. Mordon S, Devoisselle JM, Maunoury V. *In vivo* pH measurement and imaging of tumor tissue using a pH-sensitive fluorescent probe (5,6-carboxyfluorescein): instrumental and experimental studies. *Photochem. Photobiol.* 1994; 60(3): 274-279.

8. Hassan M, Riley J, Chernomordik V, Smith P, Pursley R, Lee SB, Capala J, Gandjbakhche AH. Fluorescence lifetime imaging system for *in vivo* studies. *Mol. Imaging* 2007; 6: 229-236.

9. Khramtsov VV, Grigor'ev IA, Foster MA, Lurie DJ, Nicholson I. Biological applications of spin pH probes. *Cell Mol. Biol.* 2000; 46: 1361.

10. Vavere AL, Biddlecombe GB, Spees WM, Garbow JR, Wijesinghe D, Andreev OA, Engelman DM, Reshetnyak YK, Lewis JS. A novel technology for the imaging of acidic prostate tumors by positron emission tomography. *Cancer Res.* 2009; 69: 4510-4516.

11. Gillies RJ, Raghunand N, Garcia-Martin ML, Gatenby RA. pH imaging. A review of pH measurement methods and applications in cancers. *IEEE Eng. Med. Biol. Mag.* 2004; 23(5): 57-64.

12. Gallagher FA, Kettunen MI, Day SE, Hu DE, Ardenkjaer-Larsen JH, Zandt R, Jensen PR, Karlsson M, Golman K, Lerche MH, Brindle KM. Magnetic resonance imaging of pH *in vivo* using hyperpolarized <sup>13</sup>C-labelled bicarbonate. *Nature* 2008; 453: 940-943.

13. Yoo B, Pagel MD. An overview of responsive MRI contrast agents for molecular imaging. *Front. Bioscience* 2008; 13: 1733-1752.

14. Raghunand N, Zhang S, Sherry AD, Gillies RJ. *In vivo* magnetic resonance imaging of tissue pH using a novel pH-sensitive contrast agent, GdDOTP-4Amp. *Acad. Radiol.* 2002; 9(2): S481-S483.

15. Raghunand N, Howison C, Sherry AD, Zhang S, Gillies RJ. Renal and systemic pH imaging by contrast-enhanced MRI. *Magn. Reson. Med.* 2003; 49: 249-257.

16. Garcia-Martin ML, Martinez GV, Raghunand N, Sherry AD, Zhang S, Gillies RJ. High resolution pHe imaging of rat glioma using pH-dependent relaxivity. *Magn. Reson. Med.* 2006; 55(2): 309-315.

17. Aime S, Fedeli F, Sanino A, Terreno EA. R-2/R-1 ratiometric procedure for a concentration-independent, pH-responsive, Gd(III)-based MRI agent. *J. Am. Chem. Soc.* 2006; 128: 11326–11327.
18. Martinez GV, Zhang X, Garcia-Martin ML, Morse DL, Woods M, Sherry AD, Gillies RJ. R4.6  
Imaging the extracellular pH of tumors by MRI after injection of a single cocktail of T1 and T2 contrast agents. *NMR in Biomed.* 2011; *in press*.
19. Frullano L, Catana C, Benner T, Sherry AD, Caravan P. Bimodal MR–PET Agent for R1.3  
Quantitative pH Imaging. *Angew. Chemie Int. Ed.* 2010; 49, 2382–2384.
20. Ward KM, Balaban RS. Determination of pH using water protons and chemical exchange dependent saturation transfer (CEST). *Magn. Reson. Med.* 2000; 44(5): 799-802.
21. Longo DL, Colombo W, Dastrù W, Pogi L, Tedoldi F, Terreno E, Uggeri F, Aime S. Iopamidol as a responsive MRI-chemical exchange saturation transfer contrast agent for pH mapping of kidneys: in vivo studies in mice at 7 T. *Magn. Reson. Med.* 2011; 65(1): 202- R1.3  
211.
22. Zhang S, Merritt M, Woessner DE, Lenkinski RE, Sherry AD. PARACEST agents: R1.2  
modulating MRI contrast via water proton exchange. *Acc. Chem. Res.* 2003; 36: 783-790.
23. Terreno E, Delli Castelli D, Cravotto G, Milone L, Aime S. Ln(III)-DOTAMGly complexes: a versatile series to assess the determinants of the efficacy of paramagnetic chemical exchange saturation transfer agents for magnetic resonance imaging applications. *Invest. Radiol.* 2004; 39: 235-243.
24. Aime S, Delli Castelli D, Terreno E. Novel pH-reporter MRI contrast agents. *Angew. Chem. Int. Ed.* 2002; 41(2): 4334-4336.
25. Delli Castelli D, Terreno E, Aime S. YbIII-HPDO3A: A dual pH- and temperature- R1.3, R4.10  
responsive CEST agent. *Angew. Chemie. Int. Ed.* 2011; 50(8): 1798-1800.
26. Wu Y, Soesbe TC, Kiefer GE, Zhao P, Sherry AD. A responsive Europium(III) chelate that R1.23  
provides a direct readout of pH by MRI. *J. Am. Chem. Soc.* 2010; 132(40): 14002-14003.
27. Liu G, Lu Y, Pagel MD. Design and characterization of new irreversible responsive PARACEST MRI contrast agent that detects nitric oxide. *Magn. Reson. Med.* 2007; 58: 1249-1256.
28. Li Y, Sheth VR, Liu G, Pagel MD. A self-calibrating PARACEST MRI contrast agent that detects esterase enzyme activity. *Contrast Media Molec. Imaging* 2010; *in press*.
29. Woessner DE, Zhang S, Merritt ME, Sherry AD. Numerical solution of the Bloch equations provides insights into the optimum design of PARACEST agents for MRI. *Magn. Reson. Med.* 2005; 53(4): 790-799.
30. Englander SW, Downer NW, Teitelbaum H. Hydrogen Exchange. *Annual Review Biochem.* 1972; 41: 903-924.
31. Barksdale AD, Rosenberg A. Acquisition and interpretation of hydrogen exchange data from peptides, polymers, and proteins. *Methods of Biochemical Analysis* 1982; 28: 1-113.
32. Covington AK, Robinson RA, Bates RG. Ionization Constant of Deuterium Oxide from 5 to 50 Degrees. *J. Phys. Chem.* 1966; 70(12): 3820-3824.
33. Henkelman M, Huang X, Xiang QS, Stanisiz GJ, Swanson SD, Bronskill MJ. Quantitative interpretation of magnetization transfer. *Magn. Reson. Med.* 1993; 29(6): 759-766.
34. Aime S, Barge A, Delli Castelli D, Fedeli F, Mortillaro A, Nielsen FU, Terreno E. Paramagnetic lanthanide(III) complexes as pH-sensitive chemical exchange saturation transfer (CEST) contrast agents for MRI applications. *Magn. Reson. Med.* 2002; 47: 639-648.



35. McMahon MT, Gilad AA, Zhou J, Sun PZ, Bulte JWM, van Zijl PCM. Quantifying exchange rates in chemical exchange saturation transfer agents using the saturation time and saturation power dependencies of the magnetization transfer effects on the magnetic resonance imaging signal (QUEST and QUESP): pH calibration for poly-L-lysine and a starburst dendrimer. *Magn. Reson. Med.* 2006; 55: 836–847.
36. Woods M, Woessner DE, Sherry AD. Paramagnetic lanthanide complexes as PARACEST agents for medical imaging. *Chem. Soc. Rev.* 2006; 35: 500–511.
37. Gil S, Zaderenzo P, Cruz F, Cerdán S, Ballesteros P. Imidazol-1-ylalkanoic acids as extrinsic <sup>1</sup>H NMR probes for the determination of intracellular pH, extracellular pH and cell volume. *Bioorg. Med. Chem.* 1994; 2: 305–314.
38. Welch BL The generalization of "Student's" problem when several different population variances are involved, *Biometrika* 1947, 34(1–2): 28–35. R2.3.1
39. Ali MM, Liu G, Shah T, Flask C, Pagel MD. Using two chemical exchange saturation transfer magnetic resonance imaging contrast agents for molecular imaging studies. *Acc. Chem. Res.* 2009; 42(7): 915–924.
40. Gutowsky H, Cheng H. Determination of kinetic parameters by the frequency dependence of the NMR coalescence temperature. *J. Chem. Phys.* 1973; 63: 2439–2441.
41. Liu G, Li Y, Sheth VR, Pagel MD. Imaging in vivo extracellular pH with a single PARACEST MRI contrast agent. *Molecular Imaging 2011; in press.* R1.1, R1.10, R4.1
42. Bates RG. *Electrometric pH Determinations: Theory and Practice.* Wiley: New York, 1954.
43. Van Geet AL. Calibration of the Methanol and Glycol Nuclear Magnetic Resonance Thermometers with a Static Thermistor Probe. *Anal. Chem.* 1968; 40(14): 2227–2229.
44. Henoumont C, Laurent S, Vander Elst L. How to perform accurate and reliable measurements of longitudinal and transverse relaxation times of MRI contrast media in aqueous solutions. *Contrast Media Molec. Imaging* 2009; 4(6): 312–321.
45. van Sluis R, Bhujwala ZM, Raghunand N, Ballesteros P, Alvarez J, Cerdan S, Galons JP, Gillies RJ. In vivo imaging of extracellular pH using <sup>1</sup>H MRSI. *Magn. Reson. Med.* 1999; 41(4): 743–750.
46. Grad J, Bryant RG. Nuclear magnetic cross-relaxation spectroscopy. *J. Magn. Reson.* 1999; 90(1): 1–8.
47. Terreno E, Stancanella J, Longo D, Delli Castelli D, Milone L, Sanders HMHF, Kok MB, Uggeri F, Aime S. Methods for an improved detection of the MRI-CEST effect. *Contrast Media Molec. Imaging* 2009; 4(5): 237–247.

**Figure 1. CEST MRI agents that can measure pH.** A) 5,6-dihydrouracil (19), B) Iopamidol (20), C) Pr-DOTA-Gly<sub>4</sub> (22,23), D) Yb-DO3A-oAA (24,25).

**Figure 2. CEST spectrum of Yb-DO3A-oAA.** A CEST spectrum of 30 mM Yb-DO3A-oAA at pH 7.3 and 38.3 °C was acquired with 6 μT selective saturation for 4 seconds with a 1 ppm bandwidth in 1 ppm increments. The CEST spectrum (circles) was fitted with a single function that consisted of a sum of three Lorentzian lines (thick line). The difference between the experimental data and the fitted function (squares connected by a thin line) shows the residual errors of the line fitting process.

**Figure 3. The dependence of CEST on saturation time.** The % CEST effects of the amide (filled circles) and amine (unfilled circles) of 30 mM of Yb-DO3A-oAA were measured at pH 6.32 and 38.3 °C using 10 μT saturation power. The QUEST equation was fitted to each CEST effect (solid lines) (35). The amide/amine ratio of the CEST effects (diamonds) showed no dependence on the saturation time (the dotted line represents the linear fitting of the ratio of the CEST effects).

**Figure 4. The dependence of CEST on pH.** The % CEST effects of the A) amide and B) amine of 30 mM of Yb-DO3A-oAA were measured at 38.3 °C using 10 μT saturation power. Error bars represent the standard deviation of 3 repetitions, and some error bars are smaller than the data symbol. C) The log<sub>10</sub> of the ratio of CEST showed an excellent correlation with pH ( $R^2 = 0.88$  and a standard deviation of 0.21 pH units). The pH of subsequent studies was determined R2.1 from this correlation,  $\text{pH} = 6.34 - 2.82 [\log_{10}\{((M_0 - M_S)/M_0)_{\text{amide}} / ((M_0 - M_S)/M_0)_{\text{amine}}\}]$ .

**Figure 5. Validation of pH measurements.** A) The pH measured with CEST of Yb-DO3A-oAA at 38.3 °C had outstanding agreement with the pH measured with MR spectroscopy of R1.7 IEPA (slope = 1.00,  $R^2 = 0.99$ , standard deviation = 0.09 pH units) at the same temperature. B) R2.1 The pH measured with MR spectroscopy of IEPA had excellent agreement with the pH measured with an electrode (slope = 0.92,  $R^2 = 0.996$ , standard deviation = 0.079 pH units), indicating that the presence of Yb-DO3A-oAA did not affect the chemical shift of IEPA.

**Figure 6. The dependence of CEST on concentration.** A) The % CEST effects of the amide (filled circles) and amine (unfilled circles) of Yb-DO3A-oAA were measured at pH 7.20 and 37 °C using 10 μT saturation power over a range of concentrations. The curved lines were R1.6 calculated from the Hanes-like analysis shown in Figure 6B (see reference 39 for details). The ratio of the CEST effects (diamonds) was fit with a linear function to demonstrate that the ratio is independent of concentration. B) The high  $R^2$  correlation coefficients of the linear fit of the R1.6 Hanes-like analysis method to the experimental data indicated that the chemical exchange of the amide (filled circles) or amine (unfilled circles) with water can be approximated to be a two-pool model. C) The pH values measured from the CEST effects of Yb-DO3A-oAA were independent of concentration. The dashed line represents the pH measured with an electrode.

**Figure 7. The dependence of CEST on T<sub>1</sub> relaxation time.** A) The % CEST effects of the amide (filled circles) and amine (unfilled circles) of 30 mM of Yb-DO3A-oAA were measured at pH 7.20 and 37 °C using 10 μT saturation power. Samples were doped with Gd-DTPA to modify the T<sub>1</sub> relaxation time. Although each CEST effect was dependent on T<sub>1</sub>, the ratio of the

CEST effects were relatively independent of  $T_1$ . B) The pH values measured from the CEST effects of Yb-DO3A-oAA were independent of  $T_1$ . The dashed line represents the pH measured with an electrode.

**Figure 8. The dependence of CEST on temperature.** A) The % CEST effects of the amide (filled circles) and amine (unfilled circles) of 30 mM of Yb-DO3A-oAA were measured at pH 7.30 using 10  $\mu$ T saturation power over a range of temperatures. Linear fits of each CEST effect are shown as visual aids. B) The pH values measured from the CEST effects of Yb-DO3A-oAA were strongly dependent on temperature ( $R^2 = 0.94$ , 0.068 pH units per  $^{\circ}\text{C}$ ). C) The dashed line represents the pH measured with an electrode and corrected for temperature effects.

**Figure 9. The dependence of chemical exchange measurements on pH.** The QUEST method was used to measure the chemical exchange rate,  $k_{\text{ex}}$ , from the CEST effects of the amide (filled circles) and amine (unfilled circles) of 30 mM Yb-DO3A-oAA at 38.3  $^{\circ}\text{C}$  (35). A  $\log_{10}$  axis is used to represent  $k_{\text{ex}}$  (Eq. 8). Although base-catalyzed exchange of the amide and amine should cause  $k_{\text{ex}}$  to increase as the pH is increased, the QUEST method measured lower  $k_{\text{ex}}$  values at high pH. This result indicates that the QUEST method cannot accurately measure  $k_{\text{ex}}$  at high pH values for Yb-DO3A-oAA.

**Figure 10. The dependence of CEST characteristics on pH.** A) The chemical shift of the CEST effect of the amide approached the chemical shift of water (defined as 0 ppm) as the pH was increased. B) The width of the CEST effect of the amide increased as the pH was increased. Both of these characteristics indicate MR coalescence as the pH is increased. Error bars represent the standard deviation of nine repetitions, and these results were acquired at 38.3  $^{\circ}\text{C}$ . The chemical shift and width above pH 7.5 for the CEST effect of the amide, and the chemical shift and width at all pH values for the CEST effect of the amine were limited by constraints imposed in the Lorentzian line fitting routine, so these results that may be affected by the fitting algorithm are not shown.

**Figure S1. NMR spectra of Yb-DO3AoAA.** Spectra were recorded in ~100%  $\text{D}_2\text{O}$  (top spectra) and 10%  $\text{D}_2\text{O}$  (bottom spectra) at 38.3  $^{\circ}\text{C}$ . Arrows indicate the chemical shifts of exchangeable protons.

**Figure S2. The chemical structure and NMR spectrum of 2-imidazole-1-yl-3-ethoxycarbonyl propionic acid (IEPA).** The NMR spectrum of a 40 mM sample of IEPA was acquired at pH 4.7 and 25  $^{\circ}\text{C}$ . The NMR spectral resonance of the H2 imidazole proton (8.78 ppm) was used to measure pH (37).

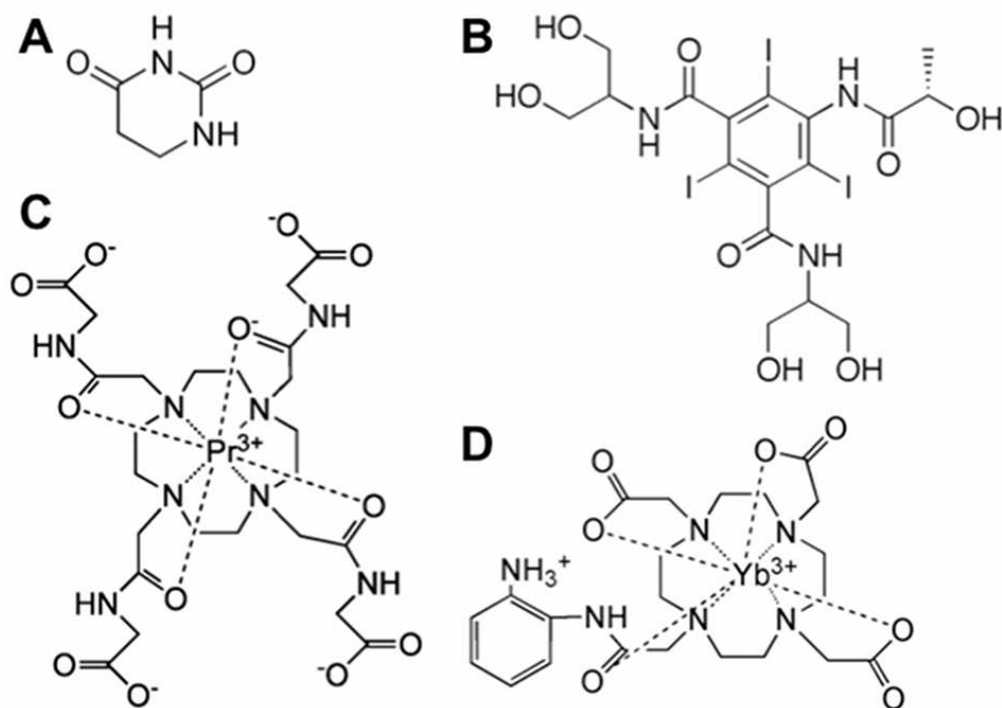


Figure 1. CEST MRI agents that can measure pH. A) 5,6-dihydrouracil (19), B) Iopamidol (20), C) Pr-DOTA-Gly4 (22,23), D) Yb-DO3A-oAA (24,25).  
79x57mm (300 x 300 DPI)

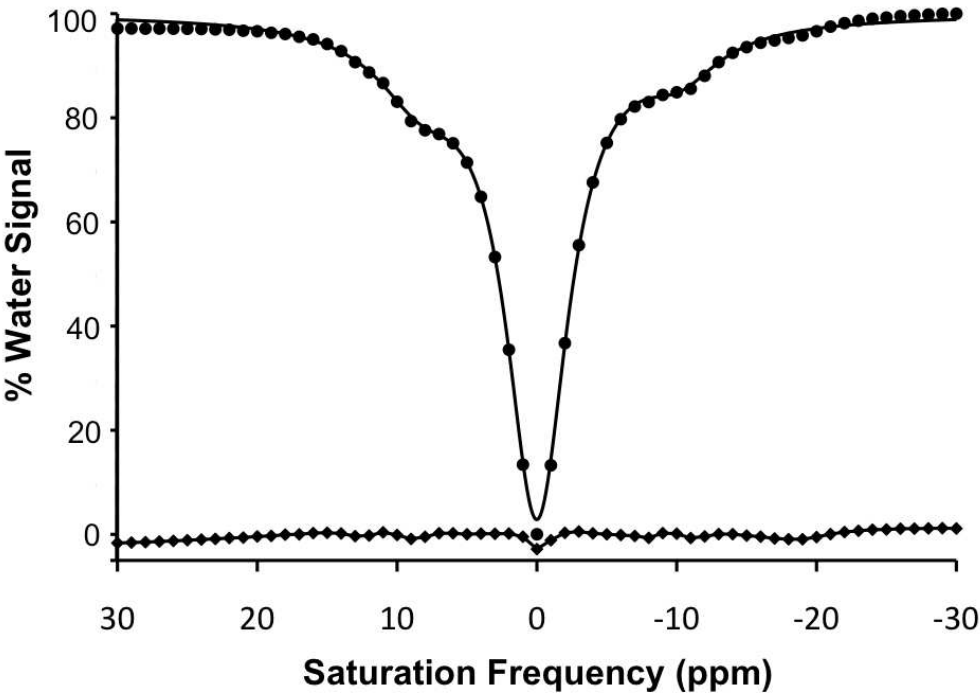


Figure 2. CEST spectrum of Yb-DO3A-oAA. A CEST spectrum of 30 mM Yb-DO3A-oAA at pH 7.3 and 38.3 °C was acquired with 6  $\mu$ T selective saturation for 4 seconds with a 1 ppm bandwidth in 1 ppm increments. The CEST spectrum (circles) was fitted with a single function that consisted of a sum of three Lorentzian lines (thick line). The difference between the experimental data and the fitted function (squares connected by a thin line) shows the residual errors of the line fitting process.

79x55mm (300 x 300 DPI)

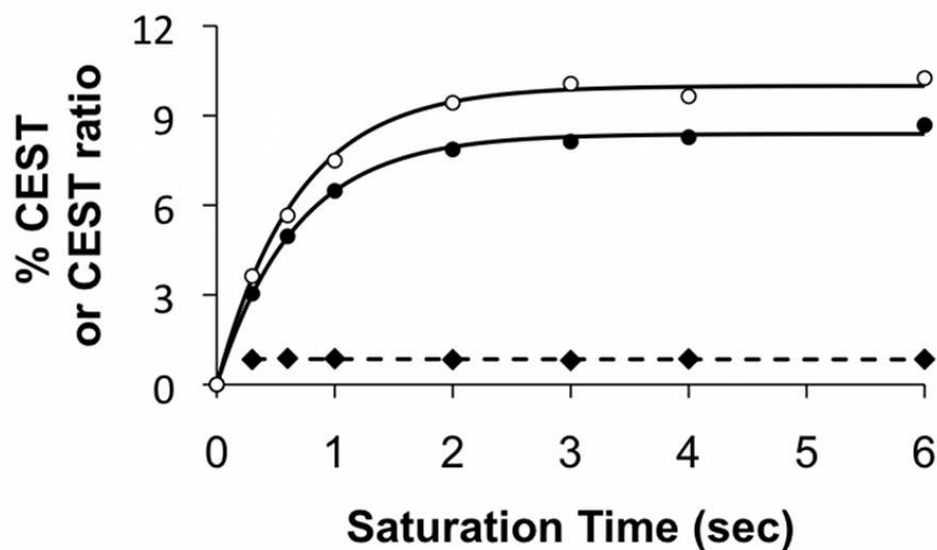


Figure 3. The dependence of CEST on saturation time. The % CEST effects of the amide (filled circles) and amine (unfilled circles) of 30 mM of Yb-DO3A-oAA were measured at pH 6.32 and 38.3 °C using 10  $\mu$ T saturation power. The QUEST equation was fitted to each CEST effect (solid lines) (35). The amide/amine ratio of the CEST effects (diamonds) showed no dependence on the saturation time (the dotted line represents the linear fitting of the ratio of the CEST effects).  
79x48mm (300 x 300 DPI)

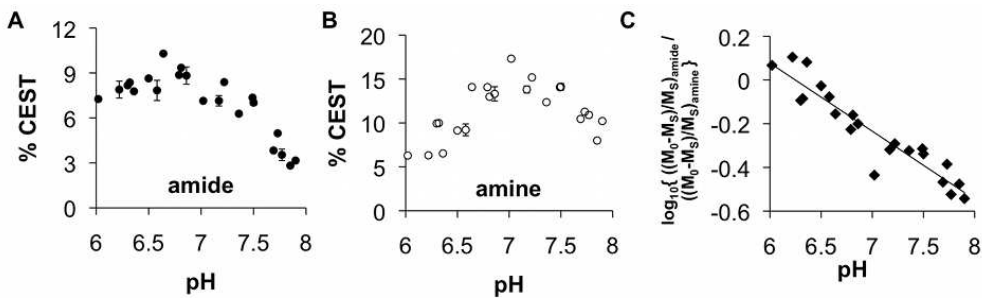


Figure 4. The dependence of CEST on pH. The % CEST effects of the A) amide and B) amine of 30 mM of Yb-DO3A-oAA were measured at 38.3 °C using 10  $\mu$ T saturation power. Error bars represent the standard deviation of 3 repetitions, and some error bars are smaller than the data symbol. C) The  $\log_{10}$  of the ratio of CEST showed an excellent correlation with pH ( $R^2 = 0.88$  and a standard deviation of 0.21 pH units). The pH of subsequent studies was determined from this correlation,  $\text{pH} = 6.34 - 2.82 [\log_{10}\{((M_0 - M_S)/M_0)_{\text{amide}} / ((M_0 - M_S)/M_0)_{\text{amine}}\}]$ .  
80x24mm (300 x 300 DPI)

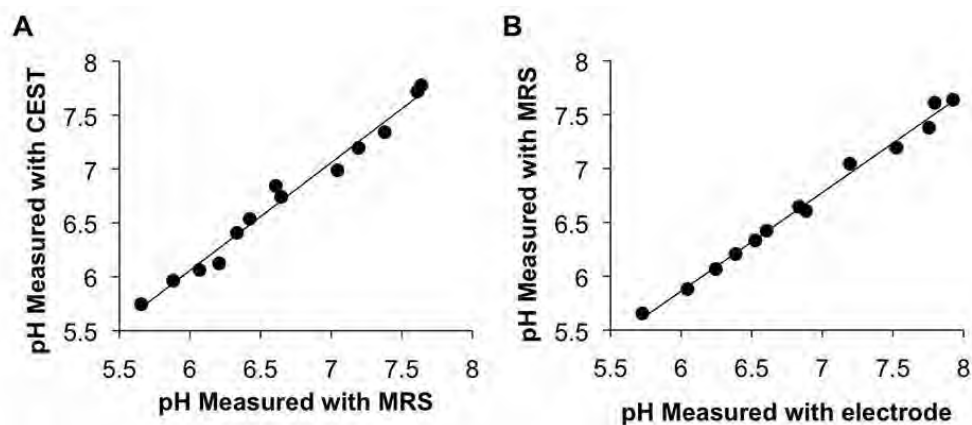


Figure 5. Validation of pH measurements. A) The pH measured with CEST of Yb-DO3A-oAA at 38.3 °C had outstanding agreement with the pH measured with MR spectroscopy of IEPA (slope = 1.00,  $R^2 = 0.99$ , standard deviation = 0.09 pH units) at the same temperature. B) The pH measured with MR spectroscopy of IEPA had excellent agreement with the pH measured with an electrode (slope = 0.92,  $R^2 = 0.996$ , standard deviation = 0.079 pH units), indicating that the presence of Yb-DO3A-oAA did not affect the chemical shift of IEPA.

80x35mm (300 x 300 DPI)



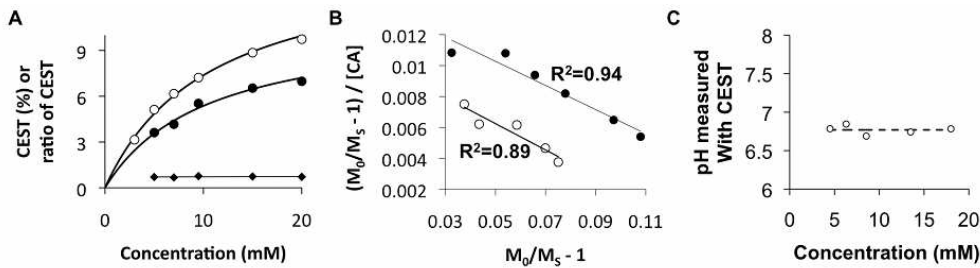


Figure 6. The dependence of CEST on concentration. A) The % CEST effects of the amide (filled circles) and amine (unfilled circles) of Yb-DO3A-oAA were measured at pH 7.20 and 37 °C using 10  $\mu$ T saturation power over a range of concentrations. The curved lines were calculated from the Hanes-like analysis shown in Figure 6B (see reference 39 for details). The ratio of the CEST effects (diamonds) was fit with a linear function to demonstrate that the ratio is independent of concentration. B) The high  $R^2$  correlation coefficients of the linear fit of the Hanes-like analysis method to the experimental data indicated that the chemical exchange of the amide (filled circles) or amine (unfilled circles) with water can be approximated to be a two-pool model. C) The pH values measured from the CEST effects of Yb-DO3A-oAA were independent of concentration. The dashed line represents the pH measured with an electrode.

79x21mm (300 x 300 DPI)

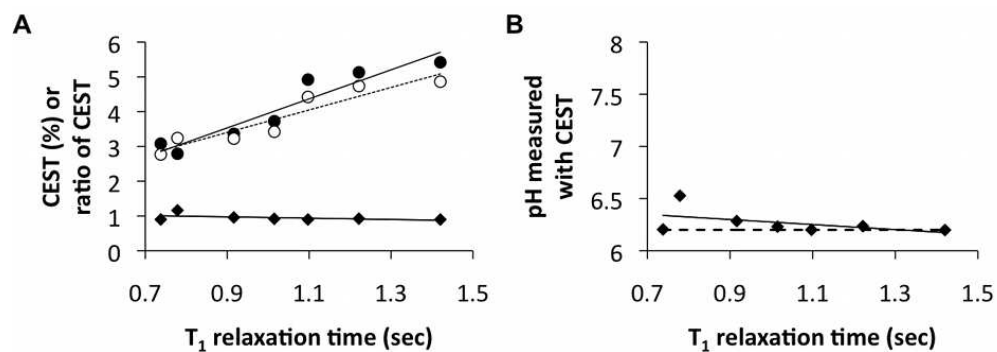


Figure 7. The dependence of CEST on  $T_1$  relaxation time. A) The % CEST effects of the amide (filled circles) and amine (unfilled circles) of 30 mM of Yb-DO3A-oAA were measured at pH 7.20 and 37 °C using 10  $\mu$ T saturation power. Samples were doped with Gd-DTPA to modify the  $T_1$  relaxation time. Although each CEST effect was dependent on  $T_1$ , the ratio of the CEST effects were relatively independent of  $T_1$ . B) The pH values measured from the CEST effects of Yb-DO3A-oAA were independent of  $T_1$ . The dashed line represents the pH measured with an electrode.

79x29mm (300 x 300 DPI)

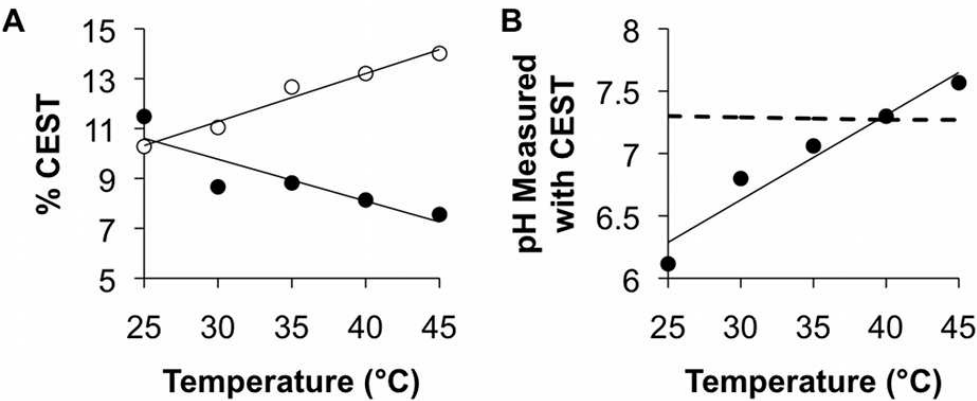


Figure 8. The dependence of CEST on temperature. A) The % CEST effects of the amide (filled circles) and amine (unfilled circles) of 30 mM of Yb-DO3A-oAA were measured at pH 7.30 using 10  $\mu$ T saturation power over a range of temperatures. Linear fits of each CEST effect are shown as visual aids. B) The pH values measured from the CEST effects of Yb-DO3A-oAA were strongly dependent on temperature ( $R^2 = 0.94$ , 0.068 pH units per  $^{\circ}\text{C}$ ). C) The dashed line represents the pH measured with an electrode and corrected for temperature effects.

79x34mm (300 x 300 DPI)

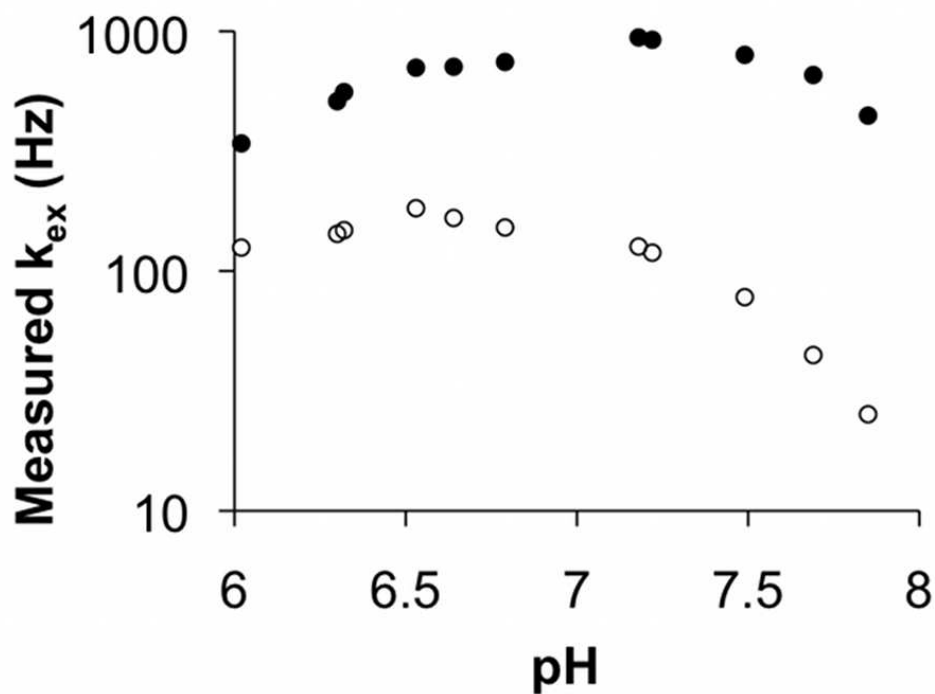


Figure 9. The dependence of chemical exchange measurements on pH. The QUEST method was used to measure the chemical exchange rate,  $k_{ex}$ , from the CEST effects of the amide (filled circles) and amine (unfilled circles) of 30 mM Yb-DO3A-oAA at 38.3 °C (35). A  $\log_{10}$  axis is used to represent  $k_{ex}$  (Eq. 8). Although base-catalyzed exchange of the amide and amine should cause  $k_{ex}$  to increase as the pH is increased, the QUEST method measured lower  $k_{ex}$  values at high pH. This result indicates that the QUEST method cannot accurately measure  $k_{ex}$  at high pH values for Yb-DO3A-oAA.

79x57mm (300 x 300 DPI)

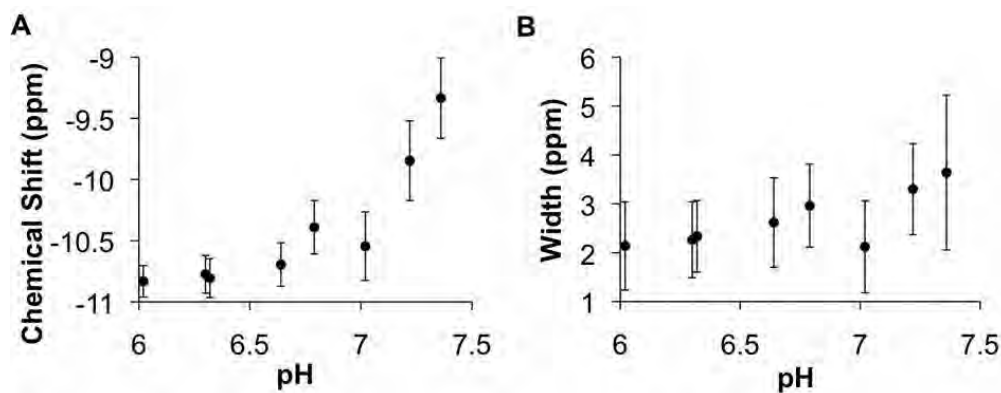


Figure 10. The dependence of CEST characteristics on pH. A) The chemical shift of the CEST effect of the amide approached the chemical shift of water (defined as 0 ppm) as the pH was increased. B) The width of the CEST effect of the amide increased as the pH was increased. Both of these characteristics indicate MR coalescence as the pH is increased. Error bars represent the standard deviation of nine repetitions, and these results were acquired at 38.3 °C. The chemical shift and width above pH 7.5 for the CEST effect of the amide, and the chemical shift and width at all pH values for the CEST effect of the amine were limited by constraints imposed in the Lorentzian line fitting routine, so these results that may be affected by the fitting algorithm are not shown.

79x31mm (300 x 300 DPI)

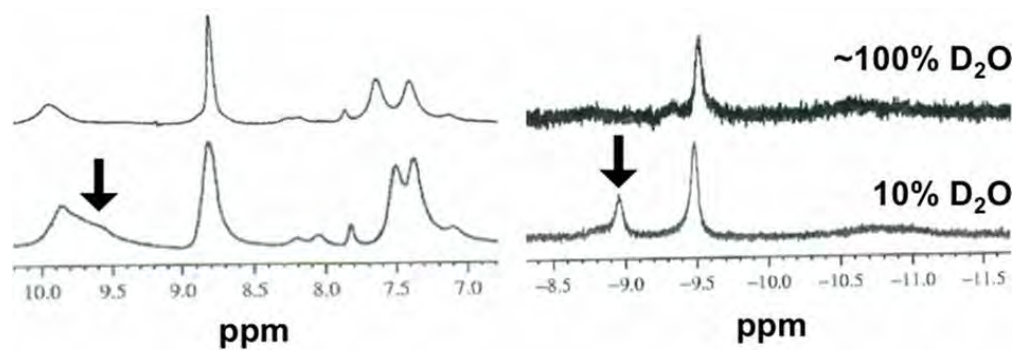


Figure S1. NMR spectra of Yb-DO3AoAA. Spectra were recorded in ~100% D<sub>2</sub>O (top spectra) and 10% D<sub>2</sub>O (bottom spectra) at 38.3 °C. Arrows indicate the chemical shifts of exchangeable protons.  
79x28mm (300 x 300 DPI)

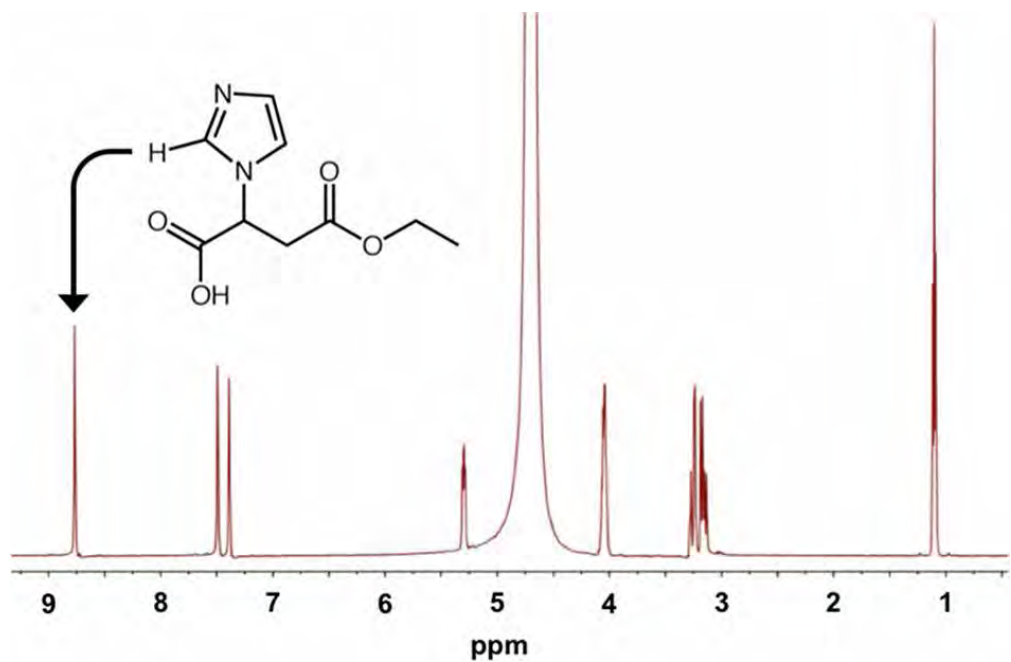


Figure S2. The chemical structure and NMR spectrum of 2-imidazole-1-yl-3-ethoxycarbonyl propionic acid (IEPA). The NMR spectrum of a 40 mM sample of IEPA was acquired at pH 4.7 and 25 °C. The NMR spectral resonance of the H2 imidazole proton (8.78 ppm) was used to measure pH (37).

79x51mm (300 x 300 DPI)

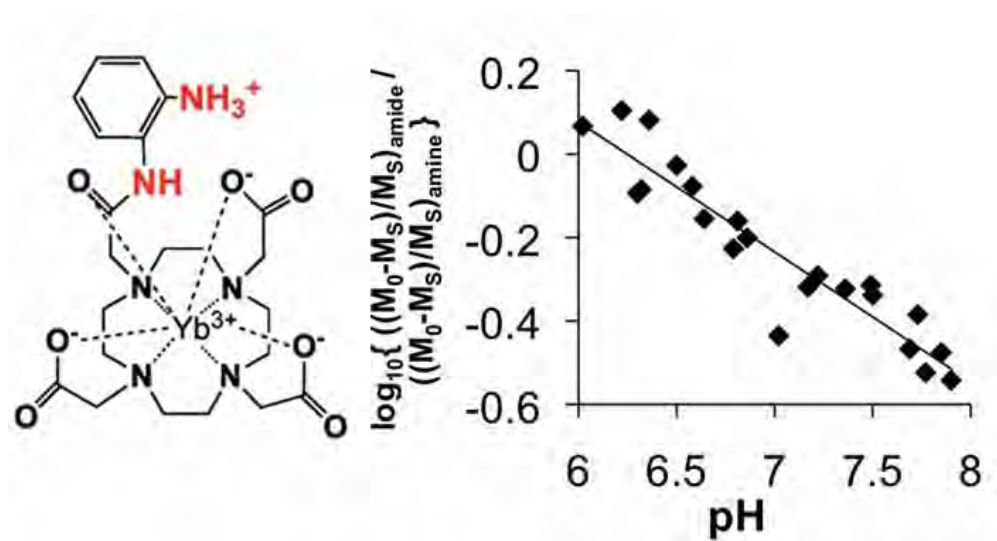


Figure for TOC  
59x31mm (300 x 300 DPI)



# Measuring In Vivo Tumor pHe With CEST-FISP MRI

Vipul R. Sheth,<sup>1</sup> Yuguo Li,<sup>2</sup> Liu Qi Chen,<sup>3</sup> Christine M. Howison,<sup>4</sup>  
Chris A. Flask,<sup>1,2</sup> and Mark D. Pagel<sup>3,5,6\*</sup>

**Paramagnetic chemical exchange saturation transfer (PARACEST) MRI contrast agents have been developed that can measure pH in solution studies, but these agents have not previously been detected in vivo. To use the PARACEST agent Yb-DO3A-oAA to measure the extracellular pH (pHe) in tumor tissue, a chemical exchange saturation transfer fast imaging with steady state precession MRI protocol was developed, the saturation period was optimized for sensitive chemical exchange saturation transfer (CEST) detection, and median filtering was used to remove artifacts in CEST spectra. These improvements were used to correlate pH with a ratio of two CEST effects of Yb-DO3A-oAA at a 7 T magnetic field strength ( $R^2 = 0.99$ , standard deviation of precision = 0.011 pH units). The PARACEST agent could not be detected in tumor tissue following i.v. injection due to the low sensitivity of in vivo CEST MRI. Yb-DO3A-oAA was detected in tumor tissue and leg muscle after directly injecting the PARACEST agent into these tissues. The measured CEST effects were used to measure a tumor pH of  $6.82 \pm 0.21$  and a leg muscle pH of  $7.26 \pm 0.14$ , and parametric pH maps were also generated from these tissue regions. These results demonstrated that tumor pHe can be measured with a PARACEST agent and a rapid CEST-MRI protocol. Magn Reson Med 000:000–000, 2011. © 2011 Wiley Periodicals, Inc.**

**Key words:** contrast agents; contrast; biophysics; technical research; molecular imaging; technique development

Some extracellular microenvironments in tumors become acidic, which changes extrinsic cellular interactions that lead to tumor malignancy (1). Extracellular acidity is toxic to surrounding host tissue, causing a breakdown of the peri-tumoral extracellular matrix that is required for invasion, and promotes the selection of metastatic cells (2–4). Therapies that alkalize tumor pHe may reduce

malignancy (2,5). A pH-modulating therapy, oral bicarbonate, can inhibit metastasis in preclinical studies and can also improve the therapeutic effect of weak-base drugs (6–8). Simplistic modeling studies suggest that short-term bicarbonate therapy is safe for clinical treatment (9), although more advanced modeling studies indicate that chronic administration of high doses of oral bicarbonate will alkalize normal tissues (10). A high resolution, noninvasive imaging methodology is needed for measuring tumor extracellular pH (pHe), so that the timing of tumor acidosis can be correlated with tumor progression and metastasis, and the effects of pH-modulating therapies can be carefully monitored.

Tumor pHe measurements have been attempted with a variety of imaging contrast agents with varying degrees of success. For example, many MR spectroscopy agents have pH-dependent chemical shifts, but MR spectroscopic imaging of these agents suffer from coarse spatial resolution (11). Hyperpolarized  $^{13}\text{C}$  MRI agents have been used to measure tumor pH, although this method requires specialized hardware that is not available in most imaging centers (12). Paramagnetic MRI contrast agents have pH-dependent relaxivities (13,14), but their pH measurements must also account for agent concentration (15). Paramagnetic chemical exchange saturation transfer (PARACEST) agents have been used to measure the accurate pH in chemical solutions (16). A chemical exchange saturation transfer (CEST) MRI protocol consists of a period of selective radiofrequency saturation that prepends a single imaging readout period so that the MR image has high spatial resolution and short acquisition times (17). In addition, PARACEST agents can be designed with chemical groups that generate selectively detectable CEST effects, so that the ratio of the two CEST effects can be exploited to remove the effect of concentration from the pH measurement (18). Therefore, CEST MRI with a PARACEST agent may improve measurements of tumor pHe for understanding tumor acidosis and monitoring pH-modulating cancer therapies.

This report describes our investigation of the translation of a PARACEST MRI agent from solution-state pH measurements to preclinical in vivo experiments. This study uses a PARACEST agent,  $\text{Yb}^{3+}$ -1,4,7,10-tetraazacyclododecane-1,4,7-triacetic acid, 10-orthoaminoanilide (Yb-DO3A-oAA), that has two active CEST sites, an amine moiety with a +10 ppm chemical shift and an amide moiety with a –10 ppm chemical shift (Fig. 1) (19–21). Because of their distinct chemical shifts, the CEST effects of these two CEST moieties are selectively detectable with spectrally selective radiofrequency saturation. Our previous studies at 600 MHz magnetic field strength

<sup>1</sup>Department of Biomedical Engineering, Case Western Reserve University, Cleveland, Ohio, USA.

<sup>2</sup>Department of Radiology, Case Western Reserve University, Cleveland, Ohio, USA.

<sup>3</sup>Department of Chemistry and Biochemistry, University of Arizona, Tucson, Arizona, USA.

<sup>4</sup>Arizona Research Laboratories, University of Arizona, Tucson, Arizona, USA.

<sup>5</sup>Department of Biomedical Engineering, University of Arizona, Tucson, Arizona, USA.

<sup>6</sup>Arizona Cancer Center, Tucson, Arizona, USA.

Grant sponsor: National Cancer Institute; Grant numbers: CA133455, CA017094; Grant sponsor: Arizona Cancer Center; Grant number: CA023074; Grant sponsor: NCI; Grant numbers: CA 017094, CA 133455-01; Grant sponsor: US Army Medical Research and Materiel Command; Grant number: W81XWH-09-1-0053; Grant sponsor: CWRU MSTP; Grant number: T32 GM007250.

\*Correspondence to: Mark D. Pagel, Ph.D., Department of Chemistry and Biochemistry, University of Arizona, Arizona Cancer Center, 1515 N. Campbell Ave., Tucson, AZ 85724-5024. E-mail: mpagel@u.arizona.edu

Received 12 January 2011; revised 17 April 2011; accepted 18 May 2011.

DOI 10.1002/mrm.23038

Published online in Wiley Online Library (wileyonlinelibrary.com).

© 2011 Wiley Periodicals, Inc.

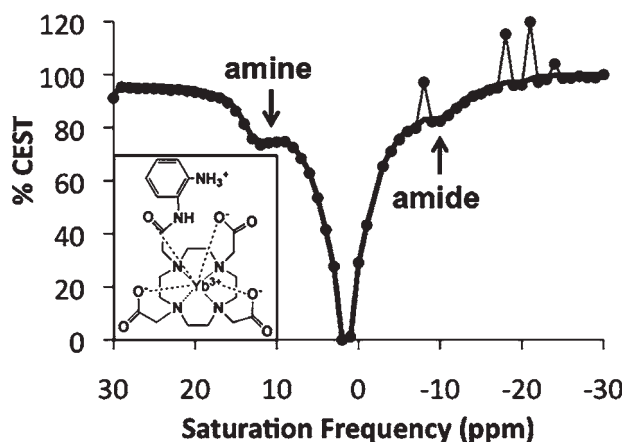


FIG. 1. A CEST spectrum of Yb-DO3A-oAA. A CEST-FISP MRI protocol was used to acquire the CEST spectrum of a phantom of 100 mM Yb-DO3A-oAA at pH 6.7 and 37°C. The median filtered spectrum (thick line) eliminated "salt and pepper" artifacts from the original spectrum (circles and thin line). The inset shows the chemical structure of Yb-DO3A-oAA.

and with a long, continuous wave saturation pulse have shown that a ratio of these CEST effects is linearly correlated with pH throughout the physiological pH range. The pH measurements with this agent are independent of concentration, endogenous  $T_1$  relaxation time, and incomplete saturation. However, a long continuous wave pulse may exceed specific absorption ratio safety limitations during in vivo studies (22). To address this concern, CEST-MRI studies are often conducted with a saturation period consisting of multiple, short, shaped pulses. Furthermore, each CEST effect of Yb-DO3A-oAA is dependent on MR coalescence because their chemical exchange rates ( $>600$  Hz at high pH) are non-negligible relative to their MR frequency difference from water ( $\pm 10$  ppm, or 6000 Hz at 600 MHz magnetic field strength). Thus, the correlation of pH and the CEST effects of this agent is sensitive to the magnetic field strength. Establishing the precision and range of a CEST ratio-pH correlation at 300 MHz magnetic field strength and with short, gaussian-shaped saturation pulses that are more practical for subsequent in vivo studies was the first aim of our study.

This report also investigates the use of fast imaging with steady state precession (FISP) MRI for in vivo tumor pHe studies. We have shown that a chemical exchange saturation transfer fast imaging with steady state precession (CEST-FISP) MRI protocol can detect CEST effects with equivalent sensitivity to CEST-spin echo studies with a much shorter acquisition time ( $\sim 5$  s/CEST-FISP acquisition) (23). Fast temporal resolution is critical for in vivo CEST MRI studies, because multiple CEST images must be acquired that differ in CEST saturation frequency to generate a CEST spectrum (24,25). In addition, this series of images must be acquired while the concentration of the PARACEST agent within the in vivo tissue does not significantly change due to pharmacokinetic wash-in or wash-out, or else a ratio of CEST effects from a single agent cannot eliminate concentration effects from the pH measurement. The ultimate goal

of this study was to determine if the rapid CEST-FISP acquisition can be coupled with a dual-moiety PARACEST agent to quantitatively measure extracellular pHe in vivo.

## MATERIALS AND METHODS

### Synthesis and Characterization of the Dual-Moiety PARACEST Agent

Our previously reported method was used to synthesize the contrast agent Yb-DO3A-oAA, and to synthesize Gd-DO3A-oAA by substituting Gd(OH)<sub>3</sub> for Yb(OH)<sub>3</sub> during the chelation step (20). The compositions of Yb-DO3A-oAA and Gd-DO3A-oAA were confirmed with ESI-MS ( $m/z$ : 688.2 (calc'd 688.2) [C<sub>22</sub>H<sub>31</sub>N<sub>6</sub>O<sub>7</sub>Yb + Na]<sup>+</sup>, 672.2 (calc'd 672.2) [C<sub>22</sub>H<sub>31</sub>N<sub>6</sub>O<sub>7</sub>Gd + Na]<sup>+</sup>). ICP-MS confirmed Yb(III) and Gd(III) solution concentrations.

To optimize pulse sequence sensitivity and to correlate CEST with pH, samples of this PARACEST agent were prepared in 25 mM piperazine-*N,N'*-bis(2-ethanesulfonic acid) (PIPES buffer) and titrated to pH values using 1–10  $\mu$ L of 6 N NaOH. In addition, PIPES buffer was then added to create samples with final volumes of 600  $\mu$ L and concentrations of 30 mM Yb-DO3A-oAA. The pH of the final solutions was measured using a calibrated pH electrode.

### Solution-State CEST-FISP MRI

Our previous report of a CEST-FISP MRI protocol used a conventional FISP MRI acquisition period (which is less sensitive to  $B_0$  inhomogeneities than a true-FISP acquisition) without fat suppression, which was preceded by a train of spectrally selective gaussian radiofrequency pulses using a Bruker Biospec 7 T MRI scanner (23). This protocol was repeated using different MR saturation frequencies to construct a CEST spectrum. The initiation of each MRI protocol required  $\sim 15$  s of "computer preparation" before the first pulse. To accomplish this study, the  $\sim 15$  s interprotocol delay was eliminated by reprogramming the FISP MRI protocol to use the "number of repetitions" loop to iterate the MR saturation frequencies that were selected by the scanner operator through a user-friendly menu. The resulting image stack greatly facilitated construction of a CEST spectrum for a region of interest (ROI) or for each pixel, which was performed with ImageJ (NIH) and Excel (Microsoft). Versions of this protocol were created with a spoiling gradient at the end of each saturation pulse or a 5 ms spoiling gradient after the entire saturation period.

The CEST-FISP MRI saturation period consisted a series of gaussian-shaped saturation pulses with a bandwidth of 300 Hz and a saturation power of 20  $\mu$ T, gradient spoiling applied at the end of the saturation period that lasted at least 2.5 ms, and a 60° FISP excitation pulse angle. Then one parameter was varied while keeping all other parameters at baseline experimental conditions. The saturation bandwidth of the gaussian pulses was varied between 60 and 1500 Hz (while maintaining a total saturation power of 20  $\mu$ T), the saturation power was varied between 5 and 30  $\mu$ T, the interpulse delay was set to 0.1 ms or 0.25 ms, the number of Gaussian

pulses was varied to create a total saturation period of 1.04–9.58 s, or the FISP excitation pulse angle was varied between 1 and 90°. The CEST effects of 100 mM Yb-DO3A-oAA were correlated with pH using our previously established procedure (21), using a saturation period with a bandwidth of 300 Hz and a saturation power of 20  $\mu$ T applied for 4.7 s, with gradient spoiling applied at the end of the saturation period, and with a 60° FISP excitation pulse angle.

### Preclinical Cancer Model

All in vivo studies were conducted according to approved procedures of the Institutional Animal Care and Use Committee of the University of Arizona. A model of MDA-MB-231 mammary carcinoma was prepared by injecting one million tumor cells in 0.5 mL of 50% Matrigel into the right lower flank of a 6-week-old female SCID mouse. MRI studies were conducted when the subcutaneous tumor reached a size greater than 4 mm in diameter. To prepare for the MRI exam, each mouse was anesthetized with 1.5–2.5% isoflurane delivered in 1 L/min oxygen gas ventilation. When needed, a 27 g catheter was inserted in the tail vein to facilitate the i.v. administration of contrast agents. The mouse was then secured to a customized MRI-compatible cradle, probes for monitoring rectal temperature and respiration were connected to the mouse, and core body temperature was regulated at 37.0°C  $\pm$  0.2°C using an automated feedback loop between the temperature probe and an air heater (SA Instruments). At the conclusion of the MRI scan, the mouse was removed from the MRI magnet and cradle and allowed to recover. At the end of the MRI studies, each mouse was euthanized with CO<sub>2</sub> asphyxiation or with i.p. administration of 0.2 mL of pentobarbital.

The contrast agents Yb-DO3A-oAA and Gd-DO3A-oAA were each injected i.v. using 50  $\mu$ L of 100 mM solutions (0.2 mmol/Kg), followed by 150  $\mu$ L of saline to “chase” the contrast agent to ensure that all of the agent was delivered. Each i.v. injection occurred slowly over 60 s to avoid excessive back-pressure in the catheter and tail vein. In a separate study, 50  $\mu$ L of 100 mM Yb-DO3A-oAA in saline was directly injected into subcutaneous tumor in one mouse and leg muscle in another mouse within 30 s at a tissue depth of 2–3 mm using a 28 g syringe. The location of the injection was guided by fiducial markers and a spin-echo MR image acquired before the injection.

### In Vivo MRI studies

Based on the conditions determined from solution-state studies, the in vivo CEST-FISP MRI study applied selective saturation with a 300 Hz bandwidth and 20  $\mu$ T power for 4.714 s, with a 1 ms interpulse delay, and a gradient spoiling applied at the end of the saturation period. FISP acquisition parameters included TR = 2.33 ms; TE = 1.16 ms; excitation flip angle = 60°; number of averages = 1; matrix = 64  $\times$  64; field of view = 4  $\times$  4 cm; in-plane spatial resolution = 625  $\times$  625  $\mu$ m; slice thickness = 3 mm. A single axial slice was acquired to visualize the tumor or leg. The temporal resolution of

acquiring one image with one selective saturation frequency was 5.10 s. A series of 61 images were acquired with selective saturation applied from –30 to 30 ppm in 1 ppm increments, which required 5.2 min. After acquiring one image series, the contrast agent Yb-DO3A-oAA was injected i.v. or directly into the tumor or leg muscle, and then six additional image series were then acquired for 31.2 min. During the study of leg muscle, two of the six image sets were not properly acquired or saved by the scanner, so that only four image sets were available.

A dynamic contrast enhancement MRI study with Gd-DO3A-oAA was also conducted using a  $T_1$ -weighted multiecho sequence. Dynamic contrast enhancement MRI acquisition parameters included TR = 250 ms; TE = 3.0 ms; excitation flip angle = 90°; matrix = 128  $\times$  128; field of view = 35  $\times$  35 mm; spatial resolution = 273  $\times$  273  $\mu$ m; slice thickness = 1 mm; two echoes per acquisition; two averages per acquisition. A contiguous series of eight axial image slices were acquired that were positioned to visualize the tumor tissue, and a second set of three contiguous axial image slices were acquired to visualize the femoral artery. Five preinjection images were acquired, the contrast agent was then injected i.v., and 60 image sets were acquired for 32.0 min with a temporal resolution of 32.0 s. The change in image contrast was used to qualitatively evaluate the agent’s pharmacokinetics within the tumor tissue.

### MR Image Analysis

To obtain a CEST spectrum from a series of CEST-FISP MR images, a ROI was manually selected for each chemical solution or in vivo tissue. CEST spectra before injection were fit using a model function with a Lorentzian line shape and a super-Lorentzian line shape using Matlab R2009B (Mathworks, Natick, MA) (26). CEST spectra after injection were fit using a model function of three Lorentzian line shapes, and the % CEST of the amine and amide of Yb-DO3A-oAA were then determined from the fitted line shapes using our previously established procedure (21). The contrast-to-noise ratio (CNR) was calculated by dividing the % CEST effect by the standard deviation of the pixel amplitudes from an empty corner of the MR image. Because % CEST is normalized to the water signal without the CEST effect, this definition of CNR is more technically known as a % CNR, but “CNR” will be used throughout this report. Pixel-wise pH maps within the tissue ROI were also calculated.

Some CEST spectra contained “salt and pepper” noise artifacts (27). These CEST spectra were median filtered by substituting the value of each data point with median value of a  $\pm 1$  point range about the data point (also known as a three-point median filter). The filtering affected the center point of the direct saturation of water in the CEST spectrum, but this original point was restored in the spectrum after filtering.

## RESULTS AND DISCUSSION

### Improvement of the Saturation Period

The contrast agent Yb-DO3A-oAA showed CEST effects at +10 ppm and –10 ppm, which agreed with previous

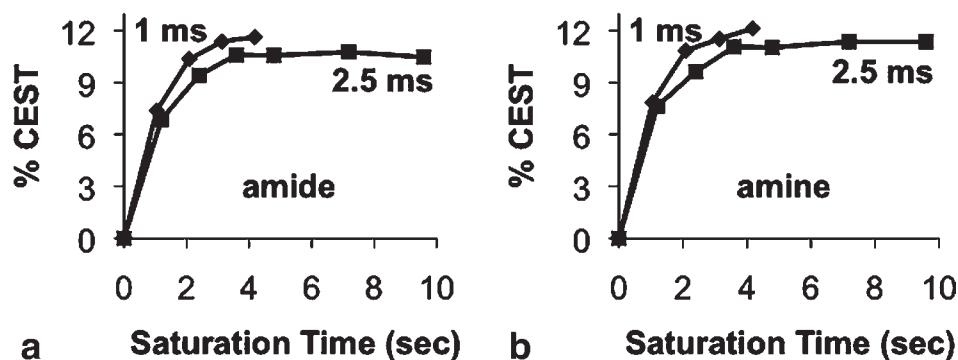


FIG. 2. The effect of interpulse time and total time during saturation. The % CEST was measured for 50 mM Yb-DO3A-oAA at pH 7.4 and 37°C. The CEST effects of the (a) amide and (b) amine were greater with a 1 ms interpulse delay (diamonds) than the 2.5 s interpulse delay (squares) and a total saturation time greater than 2.5 s reached maximum saturation.

studies (Fig. 1) (19–21). These CEST effects were maximized with saturation applied for at least 2.5 s (Fig. 2). Reducing the interpulse delay time for gradient spoiling from 2.5 to 1 ms improved the measured CEST effects, indicating that CEST detection improves with a higher duty cycle. Applying a single spoiling gradient at the end of the pulse train improved the measured CEST effects relative to gradient spoiling after each saturation pulse. The CNR of images with the different spoiling gradient methods were equal. Thus a single spoiling gradient at the end of the saturation pulse train was preferred for best CEST detection. CEST measurements were independent of a saturation bandwidth between 60 and 1500 Hz, which validated that the CEST measurements were not affected by MR frequency selectivity relative to  $B_0$  inhomogeneity (Fig. 3).

The CEST effects of Yb-DO3A-oAA increased with increasing saturation power, and did not reach a maximum CEST effect throughout the tested range of saturation powers (Fig. 4). This result did not match the behavior of a CEST agent that is instantaneously and completely saturated, in which maximum CEST would be observed at one saturation power (Eq. 1) (28). More

specifically, the maximum chemical exchange rate of the amide or amine of Yb-DO3A-oAA must not be greater than 3000 Hz (10 ppm at 300 MHz magnetic field strength) to generate a CEST effect. According to Eq. 1, the optimal saturation power for a 3000 Hz exchange rate should be 11.2  $\mu$ T, and yet greater CEST effects were observed with saturation powers that were greater than 11.2  $\mu$ T.

Instead, this result matched the behavior of a CEST agent that is incompletely saturated due to a rapid chemical exchange rate relative to the saturation power (Eq. 2) (29), which agrees with our previous reports concerning Yb-DO3A-oAA (20). This evidence for incomplete saturation indicates that the CEST-pH correlation must be performed at the saturation power to be used in subsequent in vivo studies. Our preliminary studies during the development of in vivo CEST MRI methods established that saturation powers can be lethal when applied at 40  $\mu$ T to the mouse torso or applied at 30  $\mu$ T to the mouse brain. Therefore, a saturation power level of 20  $\mu$ T was used for the remainder of this study as a compromise

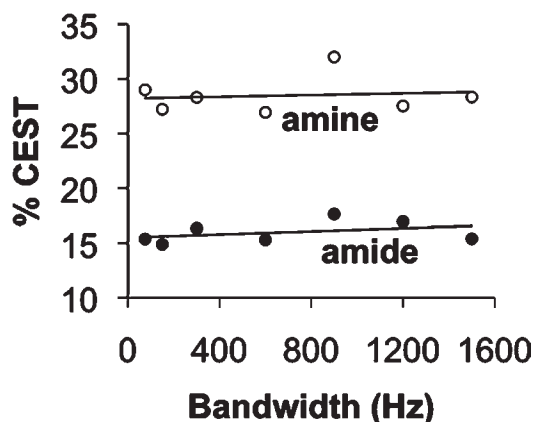


FIG. 3. The effect of saturation bandwidth. The % CEST was measured for 100 mM Yb-DO3A-oAA at pH 6.47 and 37°C. The CEST effects of the amide (filled circles) and amine (unfilled circles) relative to the saturation bandwidth showed slopes of 0.70 and 0.39% CEST per 1000 Hz, indicating that the CEST measurements were independent of saturation bandwidth.

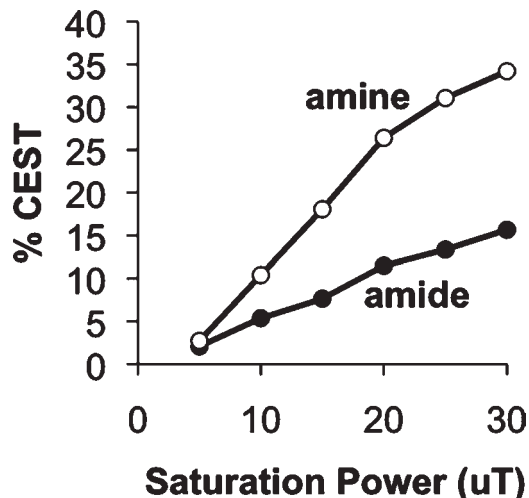


FIG. 4. The effect of saturation power. The % CEST was measured for 93 mM Yb-DO3A-oAA at pH 6.53 and 37°C and using a 3.73 s saturation period. The CEST effects of the amide (filled circles) and amine (unfilled circles) continually increased with increasing saturation power.



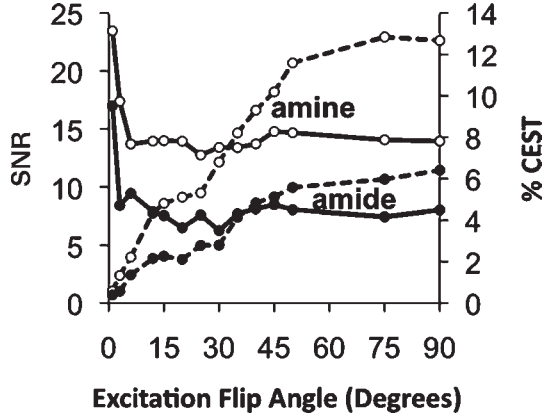


FIG. 5. The effect of the excitation pulse angle. The SNR (dashed lines) and % CEST (solid lines) were measured for the amide (filled circles) and amine (unfilled circles) for 50 mM Yb-DO3A-oAA at pH 6.47 and at 37°C. Although the greatest % CEST was observed at low pulse angles, the low SNR at these low pulse angles decreased the precision of these CEST measurements.

between generating strong CEST effects while ensuring animal safety. Using this power level, all mice were recovered from CEST MRI studies and presented no adverse symptoms.

$$B_1 = \frac{k_{\text{ex}}}{2\pi} \quad [1]$$

where  $B_1$ : saturation power (in units of Hz),  $k_{\text{ex}}$ : chemical exchange rate

$$B_1 = \frac{k_{\text{ex}}}{2\pi} \sqrt{\frac{\alpha}{1-\alpha}} \quad [2]$$

where  $\alpha$ : fraction of saturation; note that  $\alpha$  is a function of  $B_1$  so that Eqs. 1 and 2 can be compared but cannot be combined.

The magnitudes of the measured CEST effects were highest when the FISP excitation flip angle was very small (Fig. 5). Yet small flip angles created very low SNR, which can cause the CEST measurement to be imprecise. Therefore, a FISP excitation angle of 50–70° provided a good compromise between CEST magnitude and precision. Alternatively, signal averaging can be used to compensate for the decreased SNR from very small flip angles. However, the long saturation period of

CEST-FISP and the need to acquire a series of images to generate a CEST spectrum causes signal averaging to become impractical.

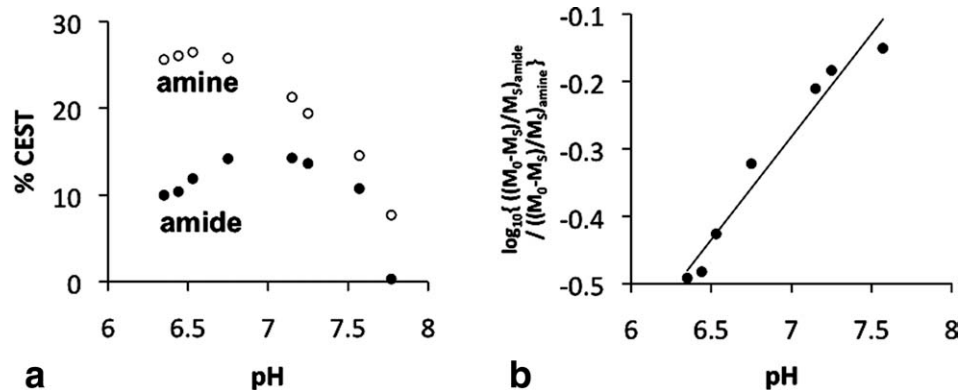
#### Calibrating CEST With pH

The correlation between CEST effects and pH for Yb-DO3A-oAA showed excellent linearity ( $R^2 = 0.99$ ), good dynamic range between 6.35 and 7.57 pH units, and outstanding precision (standard deviation of precision = 0.011 pH units; Fig. 6). This correlation at 300 MHz magnetic field strength showed a different relationship than our previous correlation performed at 600 MHz field strength. This different calibration was attributed to the lower MR frequency differences of the amide and amine relative to water at 300 MHz field strength, which caused MR coalescence to have a greater impact on CEST measurements at a lower magnetic field strength. Yet this measurable pH range at 300 MHz magnetic field strength is acceptable for studies of in vivo pHe.

#### Median Filtering

CEST spectra of solutions and tissues occasionally contained “salt and pepper” artifacts that were attributed to pulse imperfections or motion artifacts (Fig. 1). Because these artifacts occurred randomly and sparsely, median filtering was performed to remove these artifacts during the fitting process. Automated median filtering changed the value of some points in the CEST spectrum that were not artifacts. However, these adjustments were considered to be negligible, because fitting a Lorentzian line to the broad CEST peaks was not affected by a minor adjustment of one point. An exception was the narrow peak in the CEST spectrum that arose from direct saturation of water at ~0 ppm, because three-point median filtering substantially alters the peak value of a narrow spectral line that has a single data point which primarily defines the maximum of the peak and which is substantially different from its neighboring data points (27). This filtering increased the value of the point at ~0 ppm in all CEST spectra. After automated median-filtering, this substantially altered value at ~0 ppm was replaced with the original value to avoid this filtering artifact. This filtering reduced the standard deviation of repeated measurements of a single sample from 0.41 pH 0.16 pH units, which justified the use of median filtering.

FIG. 6. A CEST ratio-pH correlation for Yb-DO3A-oAA at 300 MHz magnetic field strength. **a**: The % CEST effects of the amide (filled circles) and amine (unfilled circles) of 100 mM Yb-DO3A-oAA were measured at 37°C using 20  $\mu$ T saturation power. **b**: The  $\log_{10}$  of a ratio of CEST showed an excellent correlation with pH ( $R^2 = 0.99$ ).



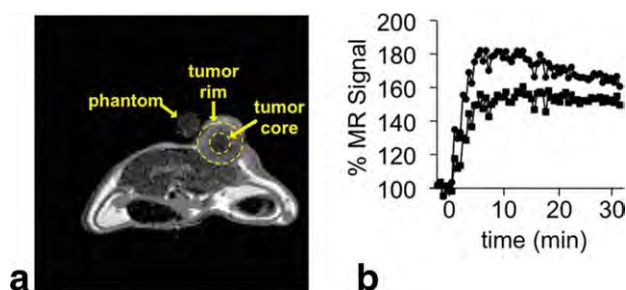


FIG. 7. Dynamic contrast enhancement MRI. After acquiring five image sets, 0.2 mmol/Kg Gd-DO3A-oAA was injected i.v. into a mouse model of MDA-MB-231 mammary carcinoma. **a:** A T1-weighted MR image at 13.87 min after injection shows good uptake of agent in the tumor rim and relatively little uptake in the tumor core. **b:** The change in image contrast after injection shows a persistent concentration of the agent from 8.27 to 32.5 min in the entire tumor (circles) and especially in the tumor rim (squares).

#### In Vivo Uptake and Pharmacokinetics of DO3A-oAA Metal Chelates

Initial i.v. injections of Yb-DO3A-oAA did not generate measurable CEST effects within tumor tissue (data not shown). CEST effects were observed in the bladder, which indicated that the injection successfully delivered agent to the blood stream. The lack of measurable CEST in tumor tissue was attributed to insufficient uptake in the tumor or rapid pharmacokinetics that was faster than the 5.2-min acquisition of a series of CEST-FISP MR images.

To investigate the pharmacokinetics of a DO3A-oAA metal chelate, a dynamic contrast enhancement MRI study was performed with Gd-DO3A-oAA (Fig. 7). The replacement of Yb(III) with Gd(III) in the contrast agent was assumed to have no effect on the pharmacokinetics of the agent. Based on the change in  $T_1$ -weighted image contrast after injection, the agent showed immediate uptake in the tumor tissue, reached a maximum concentration at 5.6 min, and then persisted in the tumor tissue throughout the 32 min scan session. This result indicated that i.v.-injected Yb-DO3A-oAA would have a steady concentration in tumor tissue during each 5.2-min acquisition of a series of CEST-FISP MR images to generate a CEST spectrum, after an initial ~5 min uptake period. Therefore, the lack of measurable CEST in tumor tissue was attributed to insufficient uptake at a typical i.v. injection concentration that was used in this study.

The persistence of Gd-DO3A-oAA in the tumor tissue was unexpected, because most small molecule MRI contrast agents typically show wash-out from tumor tissues within 20 min (30,31). An exception is MS-325, a small molecule MRI contrast agent that noncovalently binds to albumin, which shows an in vivo half-life of 2–3 h (32). Both MS-325 and Gd-DO3A-oAA are derivatives of standard lanthanide chelates that contain a ligand with at least one phenyl group. Therefore, the persistence of Gd-DO3A-oAA may possibly be caused by binding to albumin in the blood or other proteins in the tissue.

#### In Vivo CEST-FISP MRI

Due to the insufficient i.v. delivery of Yb-DO3A-oAA to tumor tissue, additional CEST-FISP MRI studies were

performed by directly injecting the contrast agent into tissues. Although direct injection created a needle track in the tissue, the injection solution did not leak from the tumor through this track, indicating that the injection volume was absorbed in the tissue. The bright image contrast following injection and without selective saturation of the agent suggested pooling of the injection volume within the tumor tissue (Fig. 8a). A ROI was manually selected for this bright image region. The CEST spectrum of the ROI showed strong CEST effects from the amide and amine that exceeded the 99% probability threshold that the change in image contrast was real (17). Because no CEST effects were observed in the image before injection (Fig. 8b), this real change in image contrast was attributed to the Yb-DO3A-oAA contrast agent. The fitting of the CEST spectrum used a single function with three Lorentzian lines (Fig. 8c). This fitting was better than fitting with a single function that included Lorentzian lines and a super-Lorentzian line shape that can account for the spectrally broad magnetization transfer (MT) effect (26). The absence of a super-Lorentzian line shape in the CEST spectrum indicated that the pooling of injection volume did not have high solid-like protein content that typically creates the MT effect (33). For comparison, the fitting of the CEST spectrum before injection included a super-Lorentzian line shape that indicated a MT effect from solid-like protein content. In addition, the widths of the fitted Lorentzian lines were greater in the tumor and muscle tissues than observed in solution, which was attributed to the  $T_2$  relaxation times of water that are likely shorter in tissue than in a solution. The peak widths from fitted Lorentzian lines (Table 1) were used to analyze the phantoms and in vivo tissues (28). The centers of the Lorentzian lines were also variables of the fitting process, which ensured that  $B_0$  inhomogeneities did not affect the results.

Both CEST effects were consistent throughout the 30 min scan session after injection of the agent, indicating that the agent was retained in the tumor (Fig. 8c). CEST effects were not observed in the bladder or tissues surrounding the tumor, which supports tumor retention of the agent. The average CEST effects from the six CEST-FISP image series were  $11.1\% \pm 2.0\%$  and  $18.9\% \pm 1.4\%$  for the amide and amine. The CEST-pH correlation (Fig. 6) was used to translate the CEST measurements into a pH measurement for the tumor ROI (Fig. 8d). The average of these six measurements was pH 6.82, which suggested that the subcutaneous tumor has a lower pH relative to normal tissues. The standard deviation of these measurements was 0.21 pH units, which indicated that the precision of in vivo pH measurements was comparable to the precision of pH measurements conducted with solution-state phantoms. A similar CEST-to-pH translation was conducted to generate a pixel-wise pH map of the tumor ROI at 23 min after injection, which showed an average pH of 6.8 and a pixel-wise standard deviation of 0.4 pH units (Fig. 8e).

Yb-DO3A-oAA was also directly injected into a mouse thigh muscle. Similar to the study of tumor tissue, the CEST-FISP MR image with no saturation of the agent showed a bright region after injection that was a better

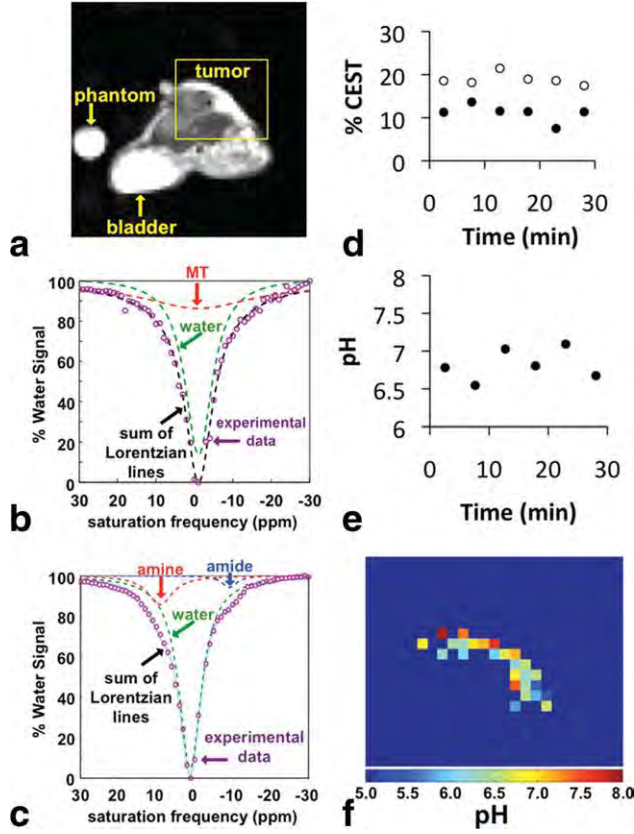


FIG. 8. Measurement of in vivo tumor pH. A 50  $\mu$ L volume of 100 mM Yb-DO3A-oAA was directly injected into the subcutaneous tumor of a model of MDA-MB-231 mammary carcinoma. **a**: A CEST-FISP MR image with selective saturation at 30 ppm (i.e., with no saturation of the contrast agent) at 23.4 min after injection shows the location of the tumor, bladder, and reference phantom. **b**: The CEST spectrum of the tumor ROI before injection shows the effects of magnetization transfer (MT) and direct saturation of water. **c**: The CEST spectrum of the tumor ROI at 23.4 min after injection shows CEST effects from the amine and amide. **d**: The CEST effects of the amide (filled circles) and amine (unfilled circles) showed that the contrast agent remained in the tumor for 28.5 min. **e**: The average pH of the tumor was determined from the CEST effects (c) and the CEST-pH calibration (Fig. 6b). The average of these six measurements was pH 6.82 with a standard deviation of 0.21 pH units. **f**: The pixel-wise pH map of the tumor ROI at 23.4 min shows an average pH of 6.8 and a pixel-wise standard deviation of 0.4 [the region shown in (f) matches the rectangular box in (a)].

match to three Lorentzian line shapes than to Lorentzian lines and a super-Lorentzian line, which suggested pooling of the injection volume (Fig. 9a,c). For comparison, the CEST spectrum of muscle before injection was best fit with a function that included a super-Lorentzian line

Table 1  
Peak Widths From Fitted Lorentzian Lines

Peak	Solution (Fig. 1) (ppm)	In vivo tumor (Fig. 8) (ppm)	In vivo muscle (Fig. 9) (ppm)
Amide	0.854	2.52	3.53
Amine	2.677	3.75	4.12
Water	2.84	3.80	4.00

shape, indicating a MT effect from solid-like protein content (Fig. 9b). This MT effect in muscle was larger than the MT effect in tumor tissue, suggesting that the muscle had more solid-like protein content than the tumor. The CEST effects within this bright region exceeded the 99% probability threshold and were attributed to the Yb-DO3A-oAA contrast agent.

The average CEST effects from the four image series of muscle translated to an average pHe of  $7.26 \pm 0.14$  pH units within muscle (Fig. 9d). Both CEST effects showed a small decrease during the first 18.2 min, suggesting some wash-out of the agent from the tissue, although this wash-out had little or no influence on the pH measurement as exemplified by the small standard deviation

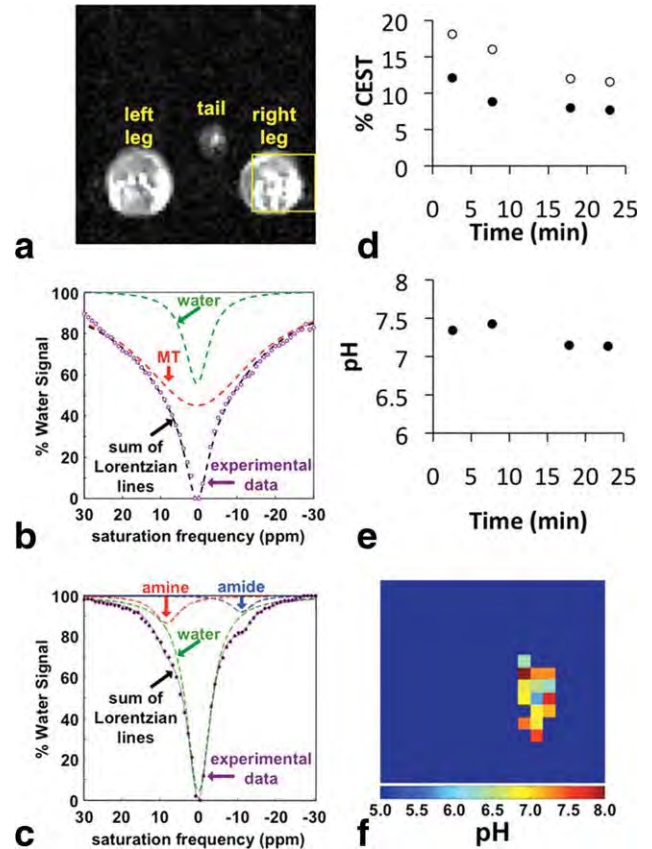


FIG. 9. Measurement of in vivo muscle pH. A 50  $\mu$ L volume of 100 mM Yb-DO3A-oAA was directly injected into the right thigh of a SCID mouse. **a**: A CEST-FISP MR image with selective saturation at 30 ppm (i.e., with no saturation of the contrast agent) at 23.4 min after injection shows the location of the legs and tail. **b**: The CEST spectrum of the tumor ROI before injection shows the effects of magnetization transfer (MT) and direct saturation of water. **c**: The CEST spectrum of the ROI of the right thigh muscle at 23.4 min after injection shows CEST effects from the amine and amide. **d**: The CEST effects of the amide (filled circles) and amine (unfilled circles) showed that the contrast agent remained in the muscle for 23.4 min. **e**: The average pH of the muscle was determined from the CEST effects (c) and the CEST-pH calibration (Fig. 6b). The average of these four measurements was pH 7.26 with a standard deviation of 0.15 pH units. **f**: The pixel-wise pH map of the tumor ROI at 23.4 min shows an average pH of 7.2 and a pixel-wise standard deviation of 0.2 pH units [the region shown in (f) matches the rectangular box in (a)].



of the four measurements (Fig. 9e). The pixel-wise pHe map of the muscle ROI at 23 min after injection showed an average pHe of 7.2 and a pixel-wise standard deviation of 0.4 pH units (Fig. 9f). These results validated that the pH measurements of the tumor were lower than the pH of normal tissues.

Direct injection of contrast agents into tissues has significant disadvantages. Although our needle insertions were comparable to clinical biopsies, needle insertion causes tissue damage and limits delivery to surface-accessible tissues. Injection of solutions into tissues may increase interstitial pressure, which may change tissue physiology. The additional solution may dilute the endogenous tissue volume and change tissue pHe. However, the consistent pHe values measured during the 30-min MRI scan session suggest that the endogenous ion content quickly equilibrated with the injection volume and was insufficient to equalize the pH measurements in tumor and muscle. Therefore, direct injection of contrast agents still had merit for these preliminary studies.

Fat suppression was not used during these studies because fat suppression via saturation can generate a MT effect that can complicate the analysis of CEST. Other fat suppression schemes, such as inversion recovery, spin-echo, and image subtraction schemes, may cause total CEST-MRI acquisition times to be impractical. Despite these disadvantages, an unsuppressed signal from fat will cause each CEST effect to be underestimated, so that the effect of fat suppression on pH measurements should be investigated in future studies. In particular, the ratio of the two CEST effects will be less sensitive to the presence of fat signal than each individual CEST effect, so that future studies may show that the ratiometric method used in this approach suppresses the influence of fat signal on the pH measurement.

This study demonstrated that exogenous PARACEST MRI contrast agents suffer from poor detection sensitivity after i.v. administration during in vivo studies. Conjugating exogenous PARACEST agents to polymers and encapsulating agents in nanocarriers have been shown to improve detection sensitivity (34–39). This approach may have potential for delivering higher concentrations of Yb-DO3A-oAA to tumor tissues via i.v. injection, although the effect of the polymer or nanocarrier on the pH measurement must be evaluated (35). Increasing the chemical shift of the amide and amine of DO3A-oAA may improve CEST detection by reducing or eliminating competition with endogenous MT effects (40). Yet a change in chemical shift will require a new CEST-pH correlation to account for the effect of MR coalescence, as demonstrated by correlations conducted at 300 and 600 MHz magnetic field strengths.

This study demonstrates that multiple CEST effects can be detected from a single PARACEST agent during an in vivo study, which can be used to determine tumor pHe with good precision. A similar study has recently been reported that measured in vivo pHe with a diamagnetic CEST agent and a CEST-MRI protocol with similar temporal resolution (41). This previous study measured pHe only in kidney tissues, because of similar problems with detection sensitivity that was encountered in our study, or also because of fast pharmacokinetic wash-in

and wash-out of the diamagnetic CEST agent. Our study demonstrates that the (PARA)CEST agent should be designed to have moderate-to-slow in vivo pharmacokinetics, such as including a phenyl moiety as exemplified by DO3A-oAA, to accommodate the modest CEST-MRI temporal resolution. Overall, our study contributes to the growing evidence that PARACEST MRI contrast agents can be used for in vivo studies, including studies of tumor pHe.

## CONCLUSIONS

An arrayed CEST-FISP MRI protocol with improved saturation conditions facilitated in vivo CEST MRI studies of tumor pHe. The interpulse delay during the saturation pulse train should be minimized, a single spoiling gradient should be applied at the end of the pulse train, and a 50–70° excitation flip angle should be employed to further improve CEST measurements with CEST-FISP MRI. The CEST effects of Yb-DO3A-oAA can measure pH throughout the physiological pH range of 6.35–7.57 at 20  $\mu$ T saturation power and 300 MHz magnetic field strength. Salt and pepper artifacts can be removed from in vivo CEST spectra by using median filtering. Although a DO3A-oAA metal chelate shows excellent retention in tumor tissue which facilitates pH measurements from CEST spectra, typical injection concentrations were insufficient to generate CEST effects from Yb-DO3A-oAA in tumor tissue. Yet direct injection of Yb-DO3A-oAA into tumor and muscle tissues circumvented the problem of poor CEST detection sensitivity. The pHe measurements showed excellent precision during the in vivo MRI scan session, and measured a lower extracellular pH in the tumor relative to muscle.

## ACKNOWLEDGMENTS

The authors thank the Experimental Mouse Shared Service of the Arizona Cancer Center for their development of the mouse tumor model. V.R.S. thanks the US Department of Defense for their support. V.R.S. was supported through the US Army Medical Research and Materiel Command and in part by the CWRU MSTP.

## REFERENCES

- Gillies RJ, Gatenby RA. Hypoxia and adaptive landscapes in the evolution of carcinogenesis. *Cancer Metastasis Rev* 2007;26:311–317.
- Gatenby RA, Gawlinski ET, Gmitro AF, Kaylor B, Gillies RJ. Acid-mediated tumor invasion: a multidisciplinary study. *Cancer Res* 2006;66:5216–5223.
- Cairns R, Papandreou I, Denko N. Overcoming physiologic barriers to cancer treatment by molecularly targeting the tumor microenvironment. *Mol Cancer Res* 2006;4:61–70.
- Gatenby RA, Gillies RJ. A microenvironmental model of carcinogenesis. *Nat Rev Cancer* 2008;8:56–61.
- Iessi E, Marino ML, Lozupone F, Fais S, De Milito A. Tumor acidity and malignancy: novel aspects in the design of anti-tumor therapy. *Cancer Ther* 2008;6:55–66.
- Robey IF, Baggett BK, Kirkpatrick ND, Roe DJ, Dosescu J, Sloane BF, Hashim AI, Morse DL, Raghunand N, Gatenby RA, Gillies RJ. Bicarbonate increases tumor pH and inhibits spontaneous metastases. *Cancer Res* 2009;69:2260–2268.
- Raghunand N, He X, van Sluis R, Mahoney B, Baggett B, Taylor CW, Paine-Murrieta G, Roe D, Bhujwalla ZM, Gillies RJ. Enhancement of chemotherapy by manipulation of tumor pH. *Br J Cancer* 1999;80:1005–1011.



8. Raghunand N, Mahoney BP, Gillies RJ. Tumor acidity, ion trapping, and chemotherapeutics. II. pH-Dependent partition coefficients predict importance of ion trapping on pharmacokinetics of weakly basic chemotherapeutic agents. *Biochem Pharmacol* 2003;66:1219–1229.
9. Silva AS, Yunes JA, Gillies RJ, Gatenby RA. The potential role of systemic buffers in reducing intratumoral extracellular pH and acid-mediated invasion. *Cancer Res* 2009;69:2677–2684.
10. Martin NK, Gaffney EA, Gatenby RA, Gillies RJ, Robey IF, PK Maini. A mathematical model of tumour and blood pHe regulation: the HCO<sub>3</sub><sup>-</sup>/CO<sub>2</sub> buffering system. *Math Biosci* 2011;230:1–11.
11. Gillies RJ, Raganand N, Garcia-Martin ML, Gatenby RA. pH Imaging. A review of pH measurement methods and applications in cancers. *IEEE Eng Med Biol Mag* 2004;23:57–64.
12. Gallagher FA, Kettunen MI, Day SE, Hu DE, Ardenkjaer-Larsen JH, Zandt R, Jensen PR, Karlsson M, Golman K, Lerche MH, Brindle KM. Magnetic resonance imaging of pH in vivo using hyperpolarized <sup>13</sup>C-labelled bicarbonate. *Nature* 2008;453:940–943.
13. Raghunand N, Howison C, Sherry AD, Zhang S, Gillies RJ. Renal and systemic pH imaging by contrast-enhanced MRI. *Magn Reson Med* 2003;49:249–257.
14. Garcia-Martin ML, Martinez GV, Raghunand N, Sherry AD, Zhang S, Gillies RJ. High resolution pHe imaging of rat glioma using pH-dependent relaxivity. *Magn Reson Med* 2006;55:309–315.
15. Martinez GV, Zhang X, Garcia-Martin ML, Morse DL, Woods M, Sherry AD, Gillies RJ. Imaging the extracellular pH of tumors by MRI after injection of a single cocktail of T1 and T2 contrast agents. *NMR Biomed*, in press.
16. Aime S, Barge A, Delli Castelli D, Fedeli F, Mortillaro A, Nielsen FU, Terreno E. Paramagnetic lanthanide(III) complexes as pH-sensitive chemical exchange saturation transfer (CEST) contrast agents for MRI applications. *Magn Reson Med* 2002;47:639–648.
17. Liu G, Ali M, Yoo B, Griswold MA, Tkach JA, Pagel MD. PARACEST MRI with improved temporal resolution. *Magn Reson Med* 2009;61:399–408.
18. Aime S, Delli Castelli D, Terreno E. Novel pH-reporter MRI contrast agents. *Angew Chem* 2002;114:4510–4512.
19. Liu G, Lu Y, Pagel MD. Design and characterization of new irreversible responsive PARACEST MRI contrast agent that detects nitric oxide. *Magn Reson Med* 2007;58:1249–1256.
20. Li Y, Sheth VR, Liu G, Pagel MD. A self-calibrating PARACEST MRI contrast agent that detects esterase enzyme activity. *Contrast Media Mol Imaging*, in press.
21. Liu G, Li Y, Sheth VR, Pagel MD. Imaging in vivo extracellular pH with a single PARACEST MRI contrast agent. *Mol Imaging*, in press.
22. Sun PZ, Benner T, Kumar A, Sorensen AG. Investigation of optimizing and translating pH-sensitive pulsed-chemical exchange saturation transfer (CEST) imaging to a 3T clinical scanner. *Magn Reson Med* 2008;60:834–841.
23. Shah T, Lu L, Dell KM, Pagel MD, Griswold MA, Flask CA. CEST-FISP: a novel technique for rapid chemical exchange saturation transfer MRI at 7 T. *Magn Reson Med* 2011;65:432–437.
24. Kim M, Gillen J, Landman BA, Zhou J, van Zijl PCM. Water saturation shift referencing (WASSR) for chemical exchange saturation transfer (CEST) experiments. *Magn Reson Med* 2009;61:1441–1450.
25. Stancanella J, Terreno E, Delli Castelli D, Cabella C, Uggeri F, Aime S. Development and validation of a smoothing-splines-based correction method for improving the analysis of CEST-MR images. *Contrast Media Mol Imaging* 2008;3:136–149.
26. Morrison C, Stanisz G, Henkelman RM. Modeling magnetization transfer for biological-like systems using a semi-solid pool with a super-Lorentzian line shape and dipolar reservoir. *J Magn Reson Series B* 1995;108:103–113.
27. Chan RH, Ho C-W, Nikolova M. Salt-and-pepper noise removal by median-type noise detectors and detail-preserving regularization. *IEEE Trans Image Process* 2005;14:1479–1485.
28. Woessner DE, Zhang S, Merritt ME, Sherry AD. Numerical solution of the Bloch equations provides insights into the optimum design of PARACEST agents for MRI. *Magn Reson Med* 2005;53:790–799.
29. Zhou J, Wilson DA, Sun PZ, Klaus JA, van Zijl PCM. Quantitative description of proton exchange processes between water and endogenous and exogenous agents for WEX, CEST, and APT experiments. *Magn Reson Med* 2004;51:945–952.
30. Tweedle MF, Wedeking P, Kumar K. Biodistribution of radiolabeled, formulated gadopentetate, gadoteridol, gadoterate, and gadodiamide in mice and rats. *Invest Radiol* 1995;30:372–380.
31. Yankeelov TE, Gore JC. Dynamic contrast enhanced magnetic resonance imaging in oncology: theory, data acquisition, analysis, and examples. *Curr Med Imaging Rev* 2007;3:91–107.
32. Parmelee DJ, Walovitch RC, Ouellet HS, Lauffer RB. Preclinical evaluation of the pharmacokinetics, biodistribution, and elimination of MS-325, a blood pool agent for magnetic resonance imaging. *Invest Radiol* 1997;32:741–747.
33. Li AX, Hudson RHE, Barrett JW, Jones CK, Pasternak SH, Bartha R. Four-pool modeling of proton exchange processes in biological systems in the presence of MRI-paramagnetic chemical exchange saturation transfer (PARACEST) agents. *Magn Reson Med* 2008;60:1197–1206.
34. Winter PM, Cai K, Chen J, Adair CR, Kiefer GE, Athey PS, Gaffney PJ, Buff CE, Robertson JD, Caruthers SD, Wickline SA, Lanza GM. Targeted PARACEST nanoparticle contrast agent for the detection of fibrin. *Magn Reson Med* 2006;56:1384–1388.
35. Pikkemaat JA, Wegh RT, Lamerichs R, van de Molengraaf RA, Langereis S, Burdinski D, Raymond AYT, Janssen HM, de Waal BFM, Willard NP, Meijer EW, Gruell H. Dendritic PARACEST contrast agents for magnetic resonance imaging. *Contrast Media Mol Imaging* 2007;2:229–239.
36. Vasalatiy O, Gerard RD, Zhao P, Sun X, Sherry AD. Labeling of adenovirus particles with PARACEST agents. *Bioconjug Chem* 2008;19:598–606.
37. Ali MM, Yoo B, Pagel MD. Tracking the relative in vivo pharmacokinetics of nanoparticles with PARACEST MRI. *Molec Pharm* 2009;6:1409–1416.
38. Terreno E, Stancanella J, Longo D, Delli Castelli D, Luciano M, Sanders HMHF, Kok M, Uggeri F, Aime S. Methods for an improved detection of the MRI-CEST effect. *Contrast Media Mol Imaging* 2009;4:237–247.
39. Wu Y, Zhao P, Kiefer GE, Sherry AD. Multifunctional polymeric scaffolds for enhancement of PARACEST contrast sensitivity and performance: effects of random copolymer variations. *Macromolecules* 2010;43:6616–6624.
40. Sherry AD, Caravan P, Lenkinski RE. Primer on gadolinium chemistry. *J Magn Reson Imaging* 2009;30:1240–1248.
41. Longo DL, Dastrù W, Digilio G, Keupp J, Langereis S, Lanzardo S, Simone Prestigio S, Steinbach O, Terreno E, Uggeri F, Aime S. Iopamidol as a responsive MRI-chemical exchange saturation transfer contrast agent for pH mapping of kidneys: in vivo studies in mice at 7 T. *Magn Reson Med* 2011;65:202–211.